Science Advances
AAAS

advances.sciencemag.org/cgi/content/full/7/10/eabf0962/DC1

Supplementary Materials for

Plasmonic nanoreactors regulating selective oxidation by energetic electrons and nanoconfined thermal fields

Chao Zhan, Qiu-Xiang Wang, Jun Yi, Liang Chen, De-Yin Wu, Ye Wang, Zhao-Xiong Xie*, Martin Moskovits*, Zhong-Qun Tian*

*Corresponding author. Email: zqtian@xmu.edu.cn (Z.-Q.T.); moskovits@chem.ucsb.edu (M.M.); zxxie@xmu.edu.cn (Z.-X.X.)

Published 5 March 2021, *Sci. Adv.* **7**, eabf0962 (2021)
DOI: 10.1126/sciadv.abf0962

This PDF file includes:

Sections S1 and S2
Figs. S1 to S48
Table S1
References

Section S1. Experimental Section

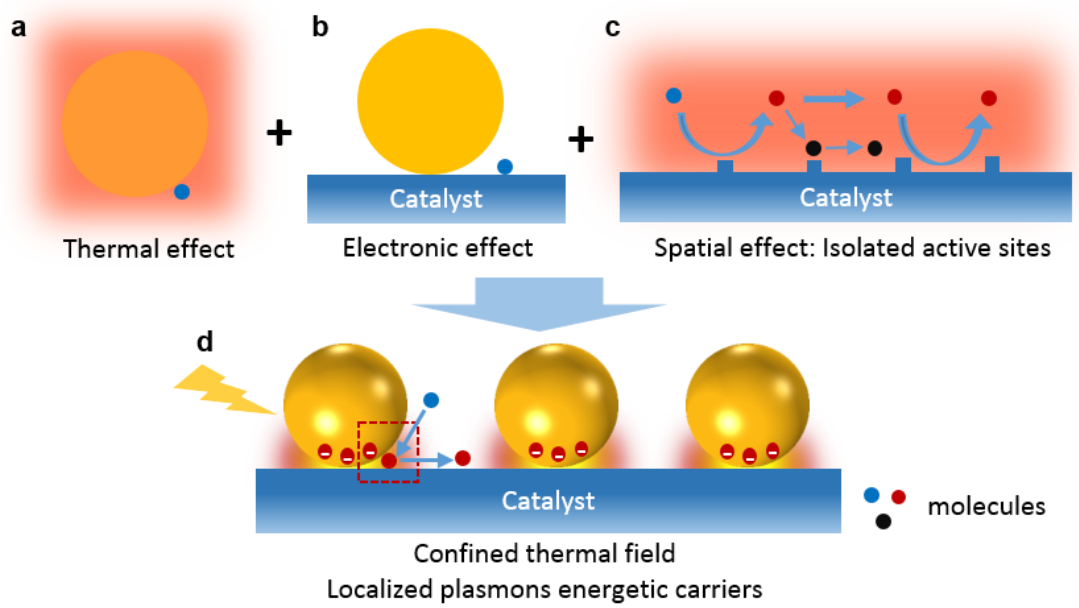

Fig. S1. Summary of plasmonic effects that may be used to improve catalytic performance. a, Thermal effect, which helps overcome an activation barrier. b, Electronic effect, which can directly influence the catalytic process. c, Spatial effect, which can isolate the active site to influence the reaction process. d, SPs are consistent with the design of hierarchical structures, thereby adding new attributes to existing catalysts so as to take advantage of all or most of the three effects a, b and c, described above. And the spatial distributions of temperature and energetic charge carriers induced by SPs is non-uniform and more local, on the nanoscale. The energetic charge carriers yielded by SPs can directly transfer to the reactants to activate them.

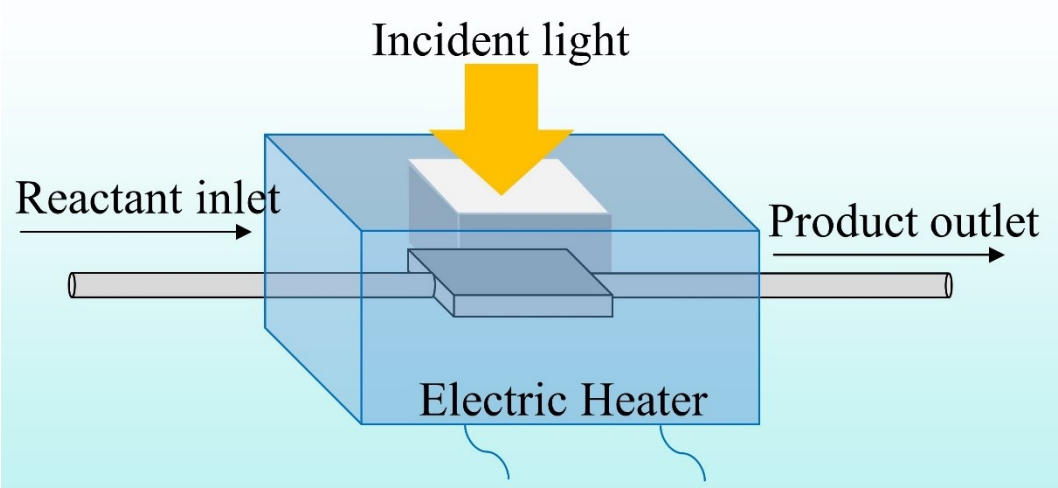

Fig. S2. Schematic of set-up and quartz glass reactor.

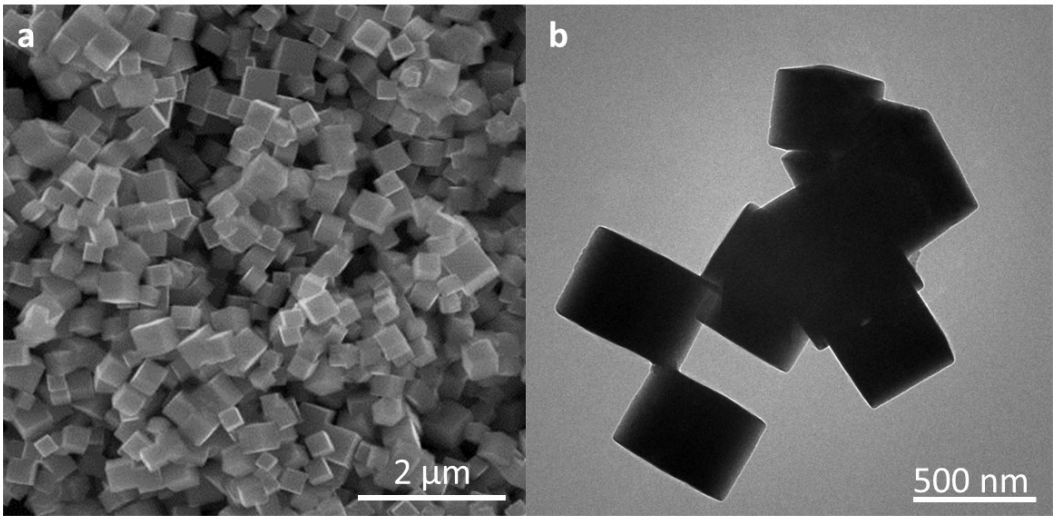

Fig. S3. SEM and TEM images of as-prepared cube Cu_2O. The images well prove the cube Cu_2O we prepared are uniform and crystallized with the (100) crystal plane exposure.

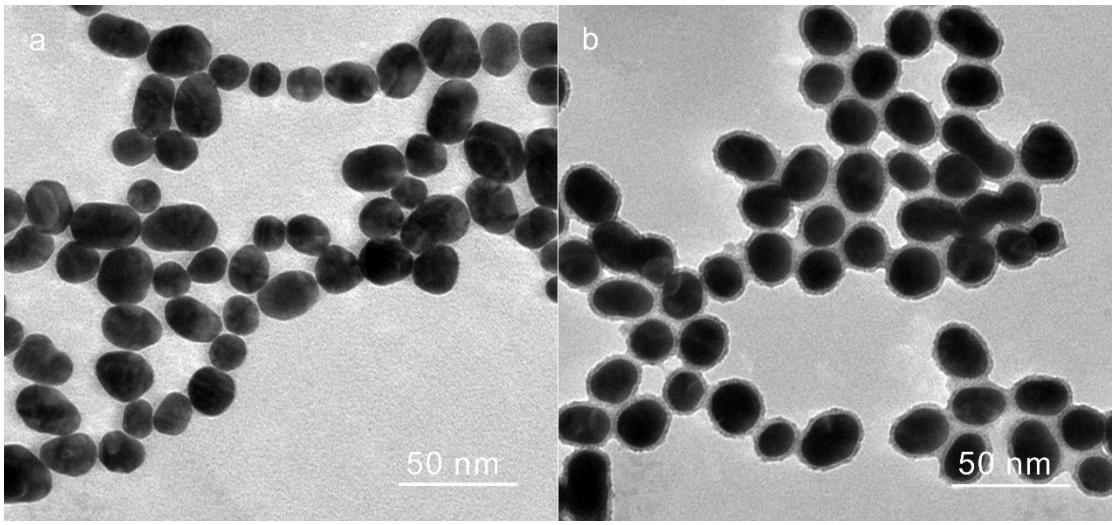

Fig. S4. TEM images of as-prepared 30 nm Au nanoparticles (a) and Au@SiO_2 nanoparticles (b). The SiO_2 shell is about 5 nm.

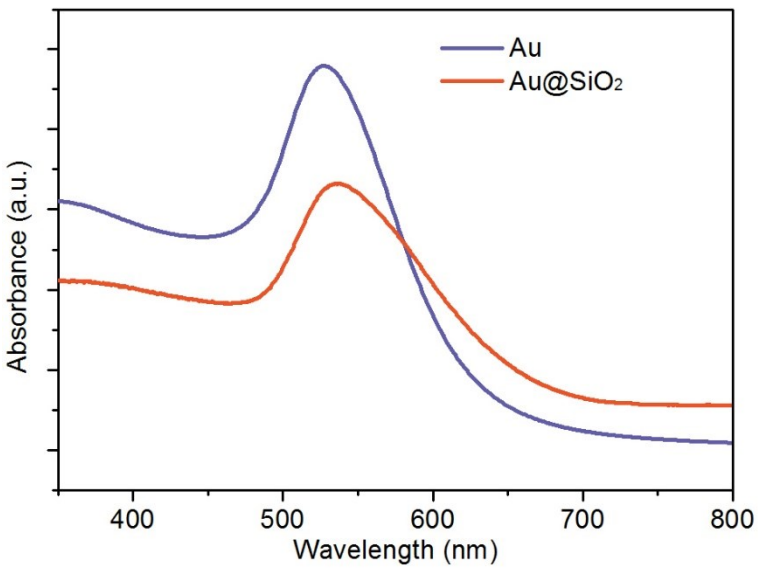

Fig. S5. Absorption spectrum of as-prepared 30 nm Au nanoparticles and Au@SiO_2 nanoparticles.

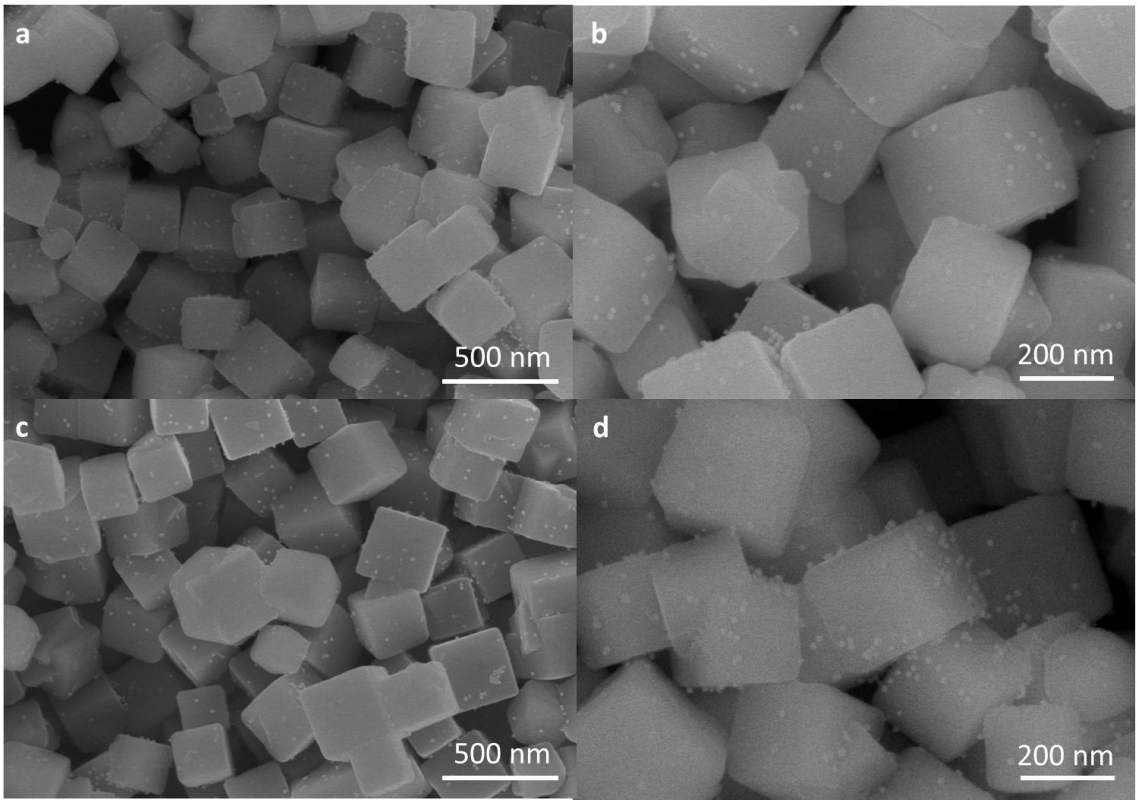

Fig. S6. SEM images of as-prepared Au-Cu_2O (a, b) and Au@SiO_2-Cu_2O (c, d) hierarchical catalysts.

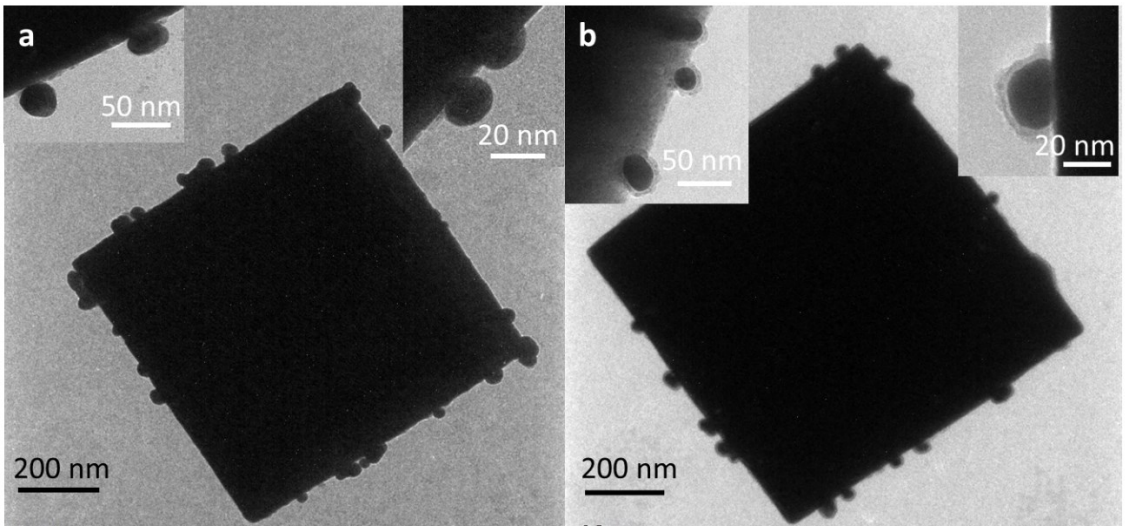

Fig. S7. TEM images of as prepared Au-Cu_2O (a) and Au@SiO_2-Cu_2O (b) hierarchical catalysts.

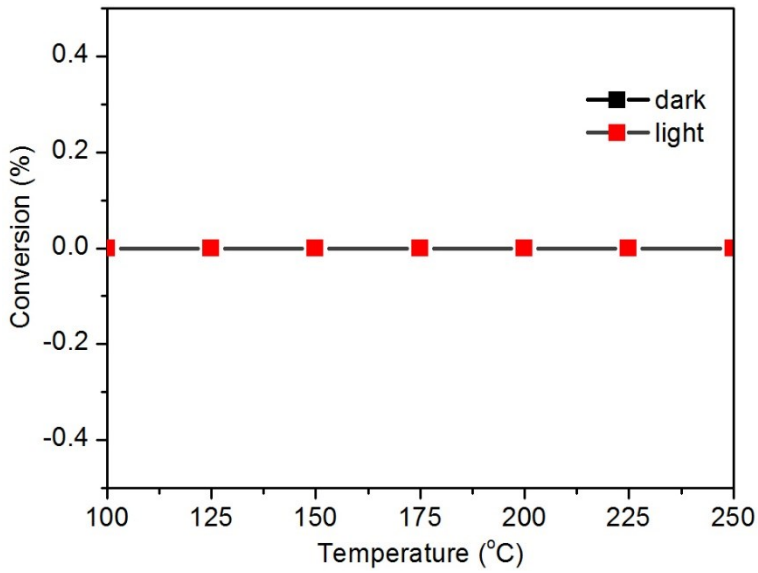

Fig. S8. Catalytic performance of Au-SiO_2 with or without illumination at different temperature. There is no obvious reaction between 100 ºC to 250 ºC.

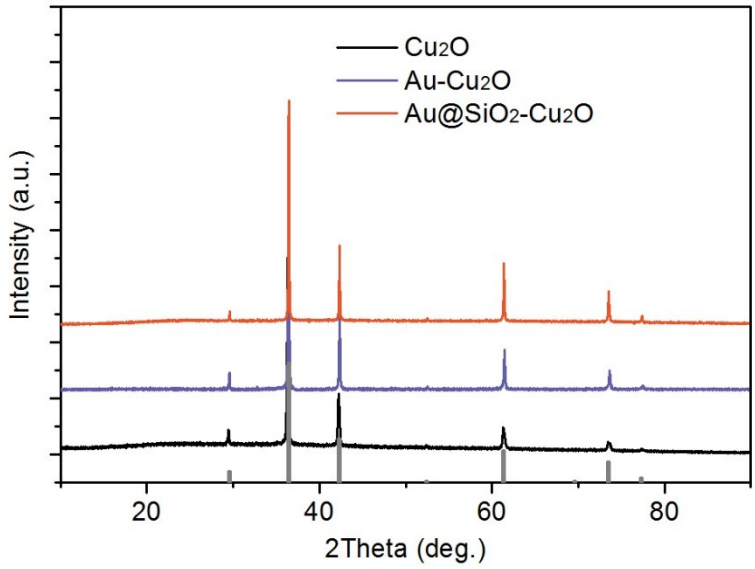

Fig. S9. XRD patterns of as prepared cube Cu_2O, Au-Cu_2O and Au@SiO_2-Cu_2O catalysts. The assemble of Au NPs or Au@SiO_2 NPs on the surface of cube Cu_2O does not affect its crystal phase.

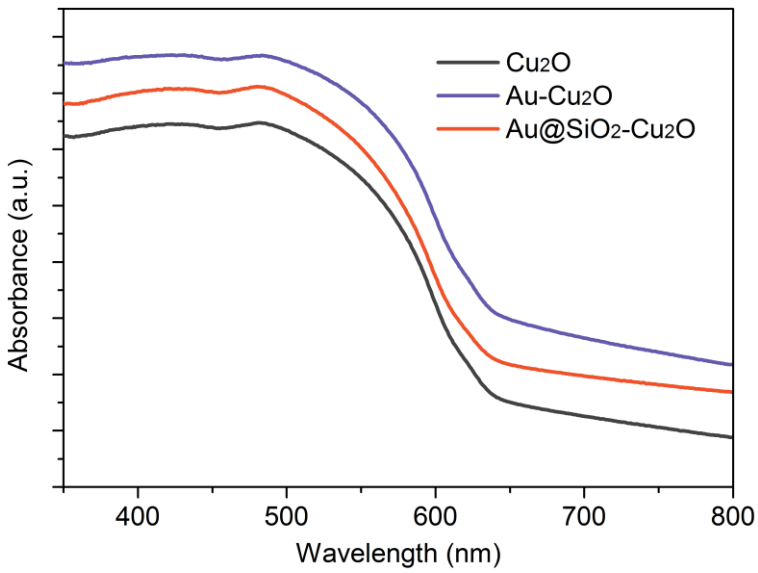

Fig. S10. Absorption spectrum of as prepared cube Cu_2O, Au-Cu_2O and Au@SiO_2-Cu_2O hierarchical catalysts.

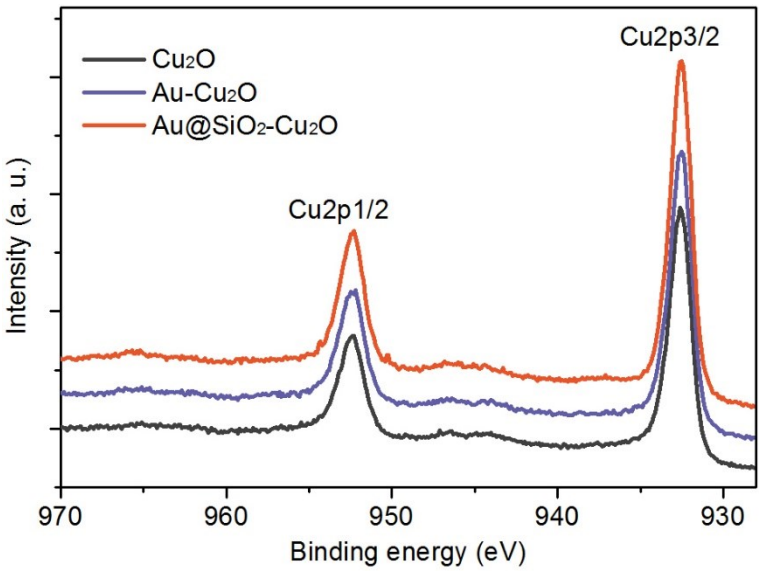

Fig. S11. XPS of Cu 2p of C-Cu_2O, Au-Cu_2O and Au@SiO_2-Cu_2O hierarchical catalysts. The Cu 2p XPS spectrum with no satellite structure to the main peaks indicates no oxidation of surface Cu^+ (*54*).

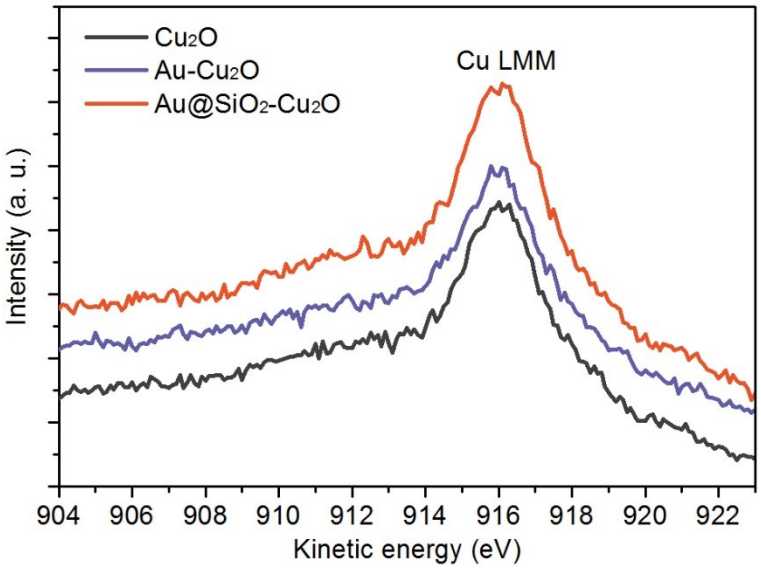

Fig. S12. XPS results of Cu LMM of C-Cu_2O, Au-Cu_2O and Au@SiO_2-Cu_2O hierarchical catalysts. Cu LMM Auger transition kinetic energy at 916.5 eV further improves the existence of Cu^+ on the surface (*54, 55*).

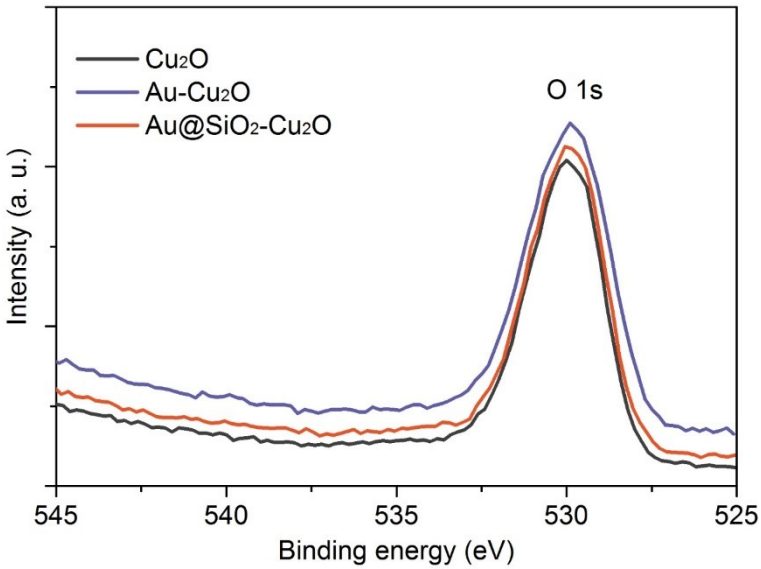

Fig. S13. XPS results of O 1s of C-Cu_2O, Au-Cu_2O and Au@SiO_2-Cu_2O hierarchical catalysts.

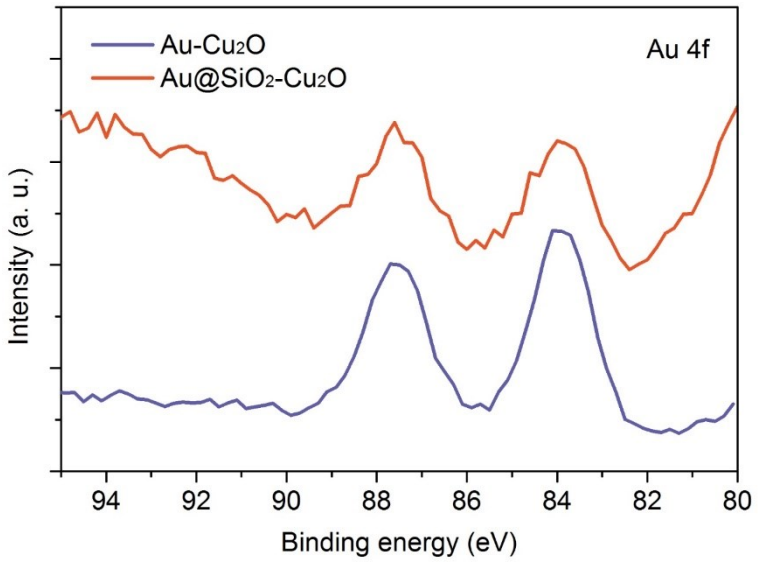

Fig. S14. XPS results of Au 4f of Au-Cu_2O and Au@SiO_2-Cu_2O hierarchical catalysts (56-*57*).

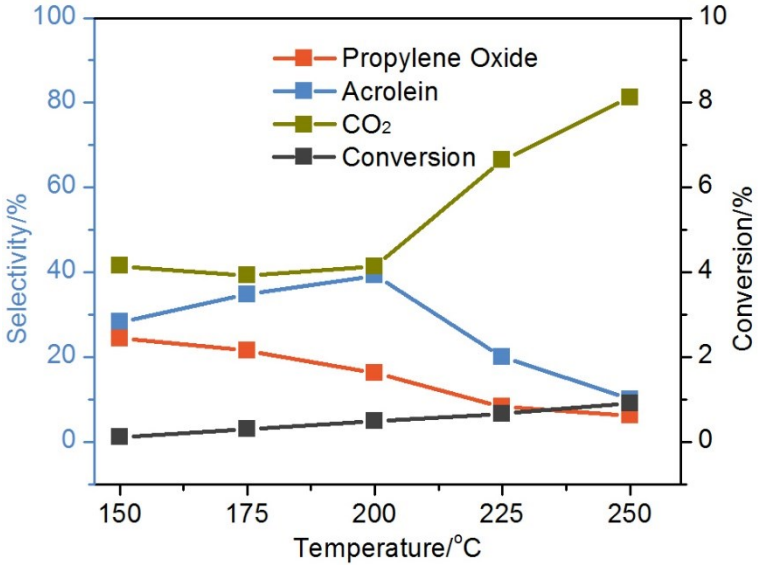

Fig. S15. Catalytic performance of surfactant free C-Cu_2O. The main product is CO_2.

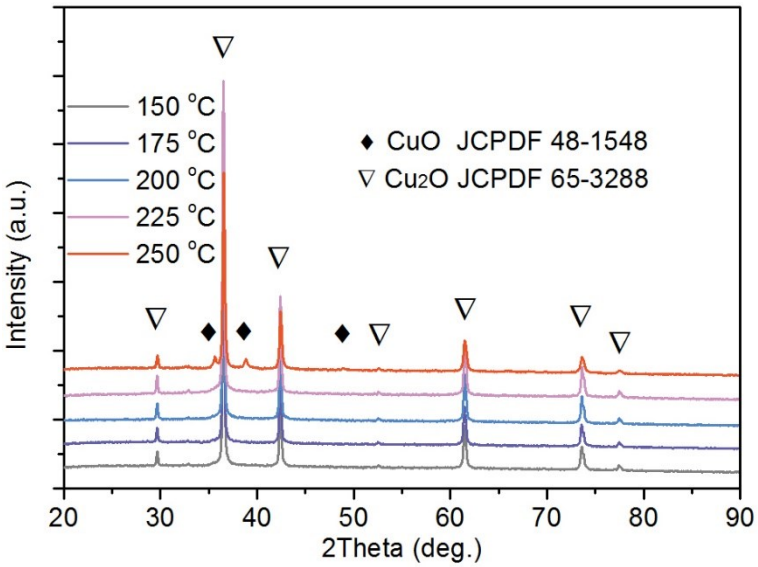

Fig. S16. XRD patterns and of C-Cu_2O after catalysis at different temperature: (a) 150 ºC, (b) 175 ºC, (c) 200 ºC, (d) 225 ºC, (e) 250 ºC. No obvious CuO peak was observed until the operated temperature was higher than 250 ºC.

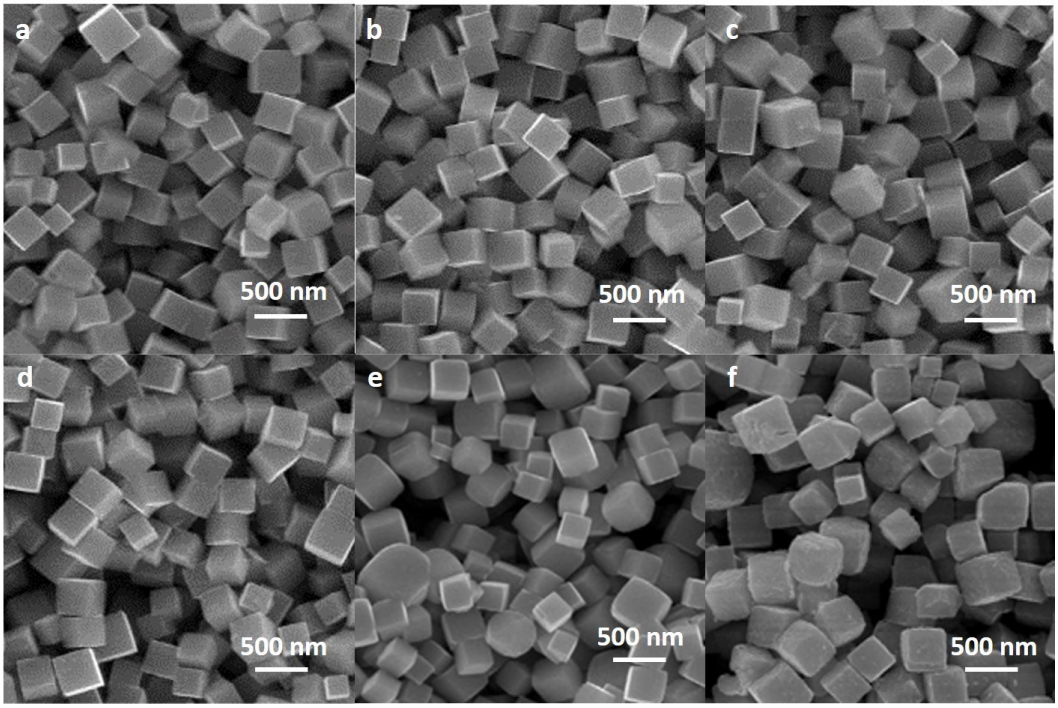

Fig. S17. SEM images of C-Cu_2O after catalysis at different temperature: (a) 125 °C, (b) 150 °C, (c) 175 °C, (d) 200 °C, (e) 225 °C, (f) 250 °C.

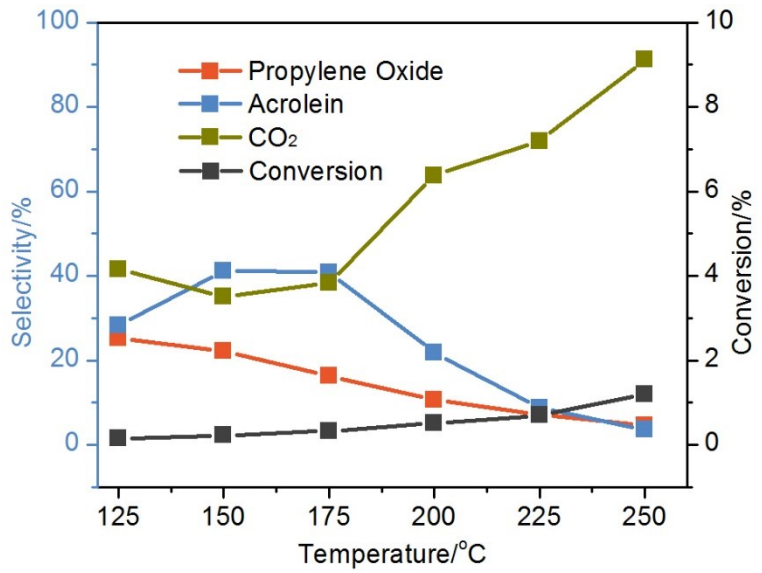

Fig. S18. Catalytic performance of surfactant free C-Cu_2O under illumination at different temperature. The main product is CO_2.

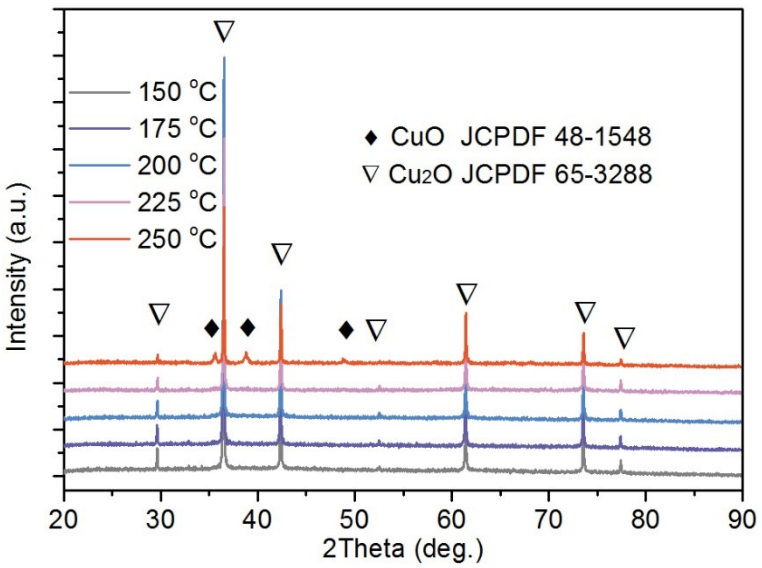

Fig. S19. XRD patterns and of C-Cu_2O after catalysis under illumination at different temperature: (a) 150 ºC, (b) 175 ºC, (c) 200 ºC, (d) 225 ºC, (e) 250 ºC. No obvious CuO peak was observed until the operated temperature was higher than 250 ºC.

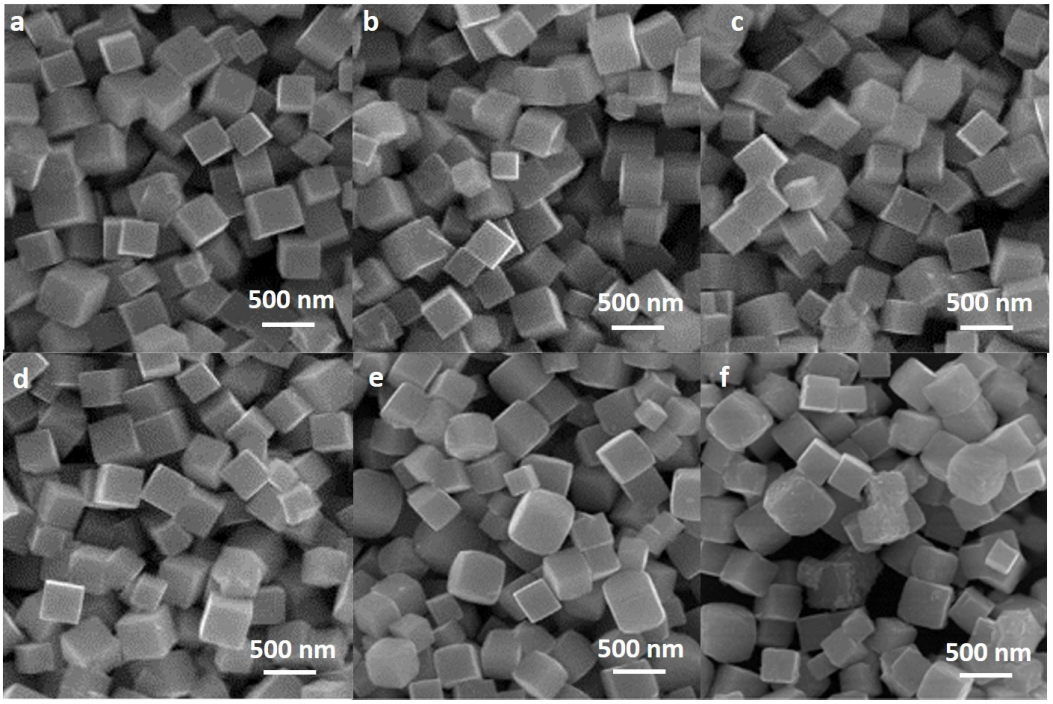

Fig. S20. SEM images of C-Cu_2O after catalysis under illumination at different temperature: (a) 125 °C, (b) 150 °C, (c) 175 °C, (d) 200 °C, (e) 225 °C, (f) 250 °C.

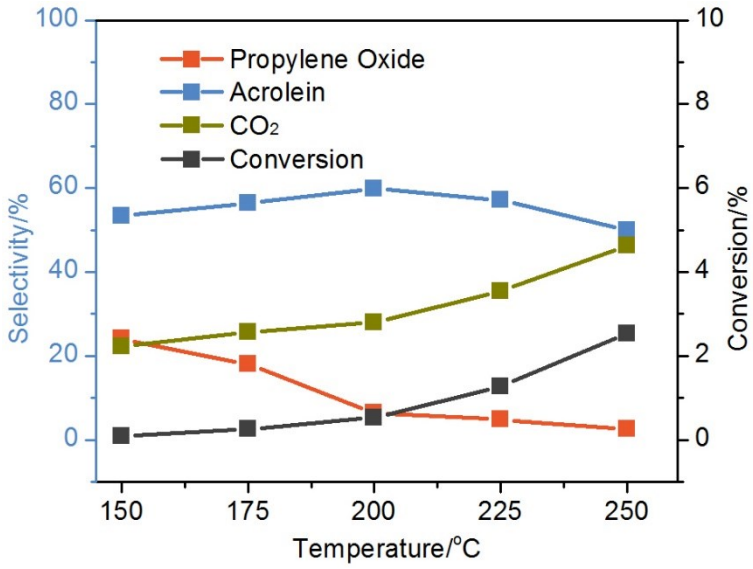

Fig. S21. Catalytic performance of Au-Cu_2O at different temperature. The main product is acrolein.

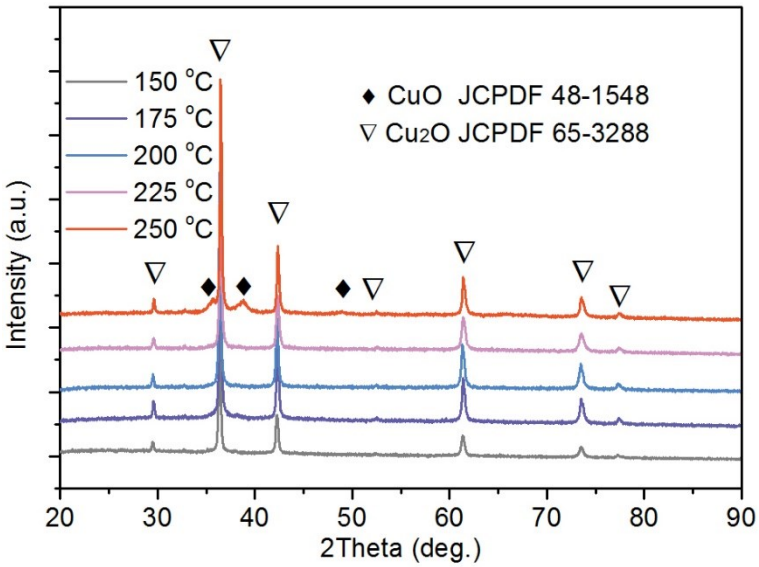

Fig. S22. XRD patterns and of Au-Cu_2O after catalysis at different temperature: (a) 150 ºC, (b) 175 ºC, (c) 200 ºC, (d) 225 ºC, (e) 250 ºC. No obvious CuO peak was observed until the operated temperature was higher than 250 ºC.

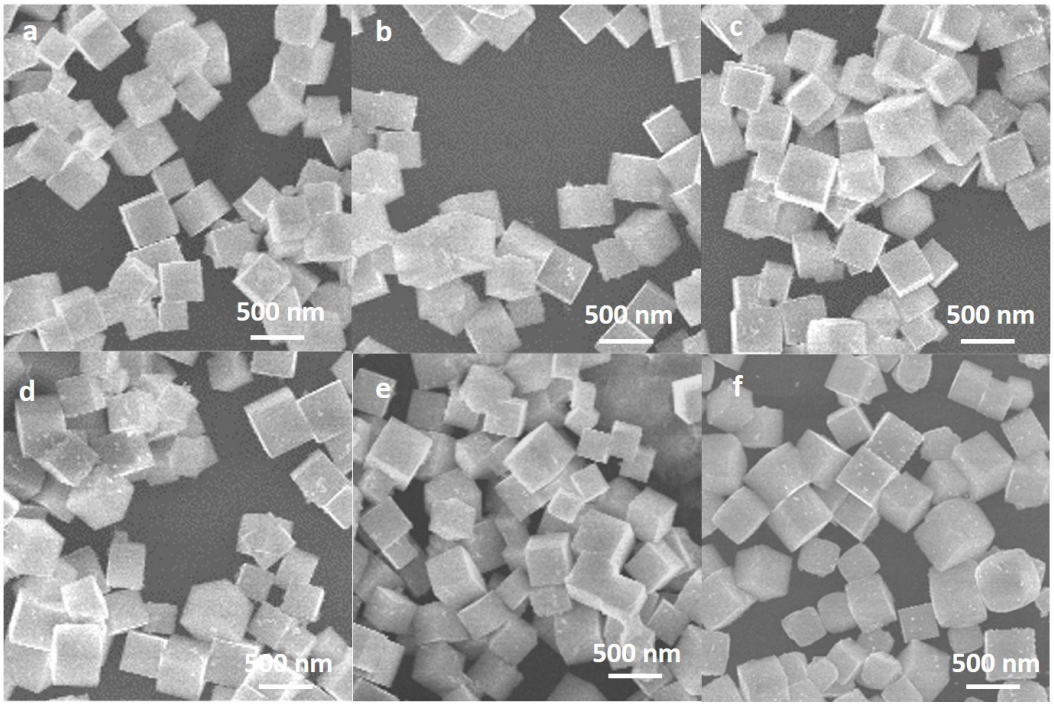

Fig. S23. SEM images of Au-Cu_2O after catalysis at different temperature: (a) 125 °C, (b) 150 °C, (c) 175 °C, (d) 200 °C, (e) 225 °C, (f) 250 °C.

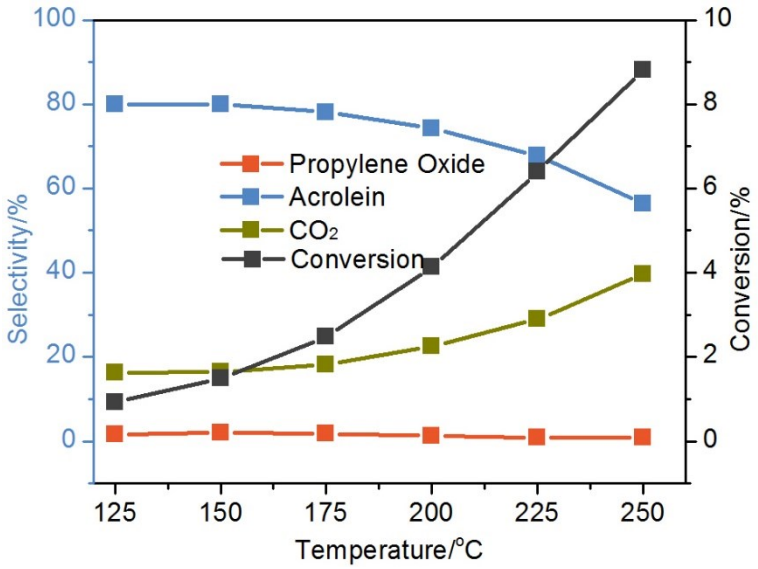

Fig. S24. Catalytic performance of Au-Cu_2O under illumination at different temperature. The main product is acrolein.

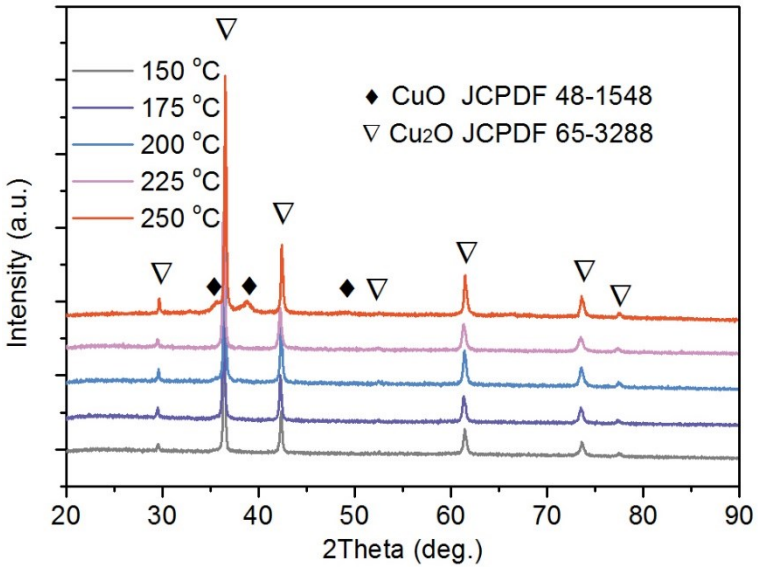

Fig. S25. XRD patterns and of Au-Cu_2O after catalysis under illumination at different temperature: (a) 150 °C, (b) 175 °C, (c) 200 °C, (d) 225 °C, (e) 250 °C. No obvious CuO peak was observed until the operated temperature was higher than 250 °C.

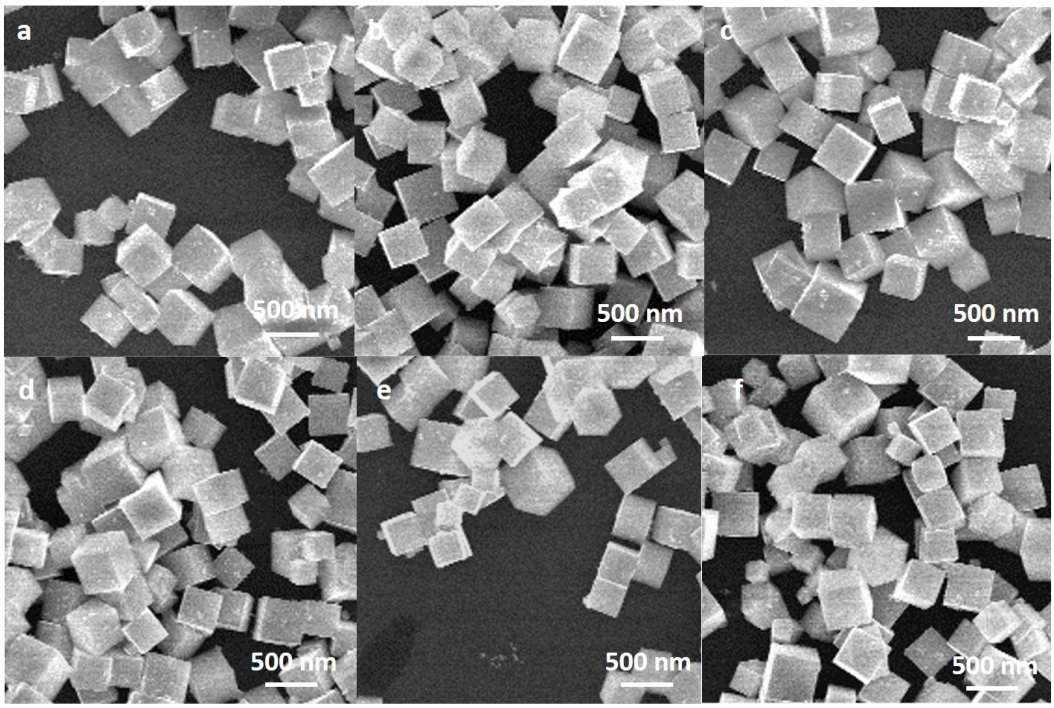

Fig. S26. SEM images of Au-Cu_2O after catalysis under illumination at different temperature: (a) 125 °C, (b) 150 °C, (c) 175 °C, (d) 200 °C, (e) 225 °C, (f) 250 °C.

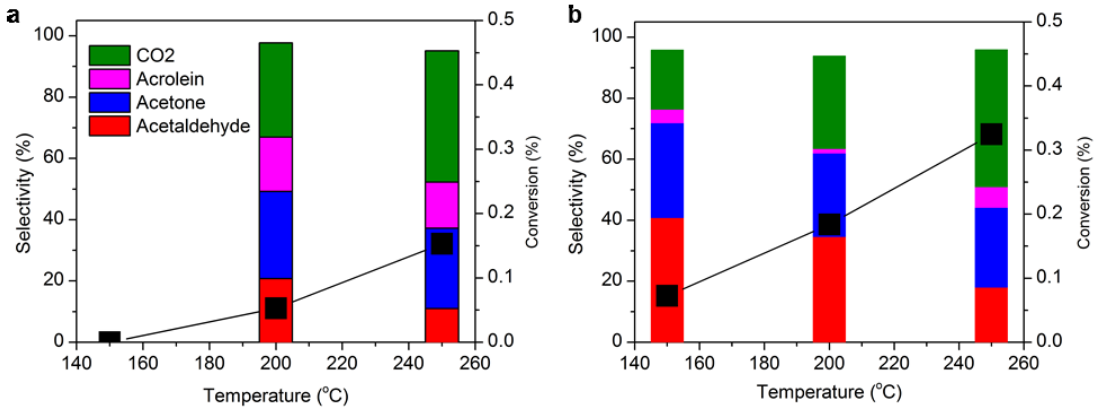

Fig. S27. Catalytic performance of Au-TiO_2 without (a) and with (b) illumination of visible light.

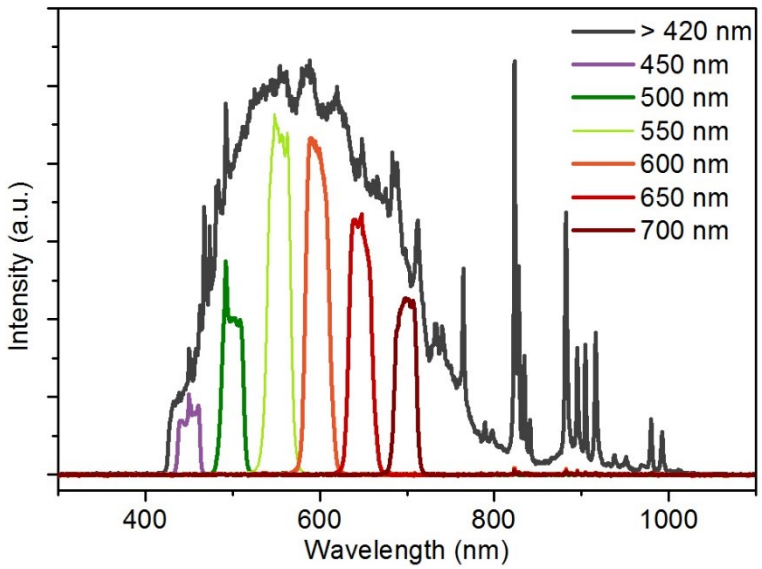

Fig. S28. Spectrum of the light source with 420 nm long-pass filter, and 450 nm, 500 nm, 550 nm, 600 nm, 650 nm, 700 nm band-pass filters (5*8*).

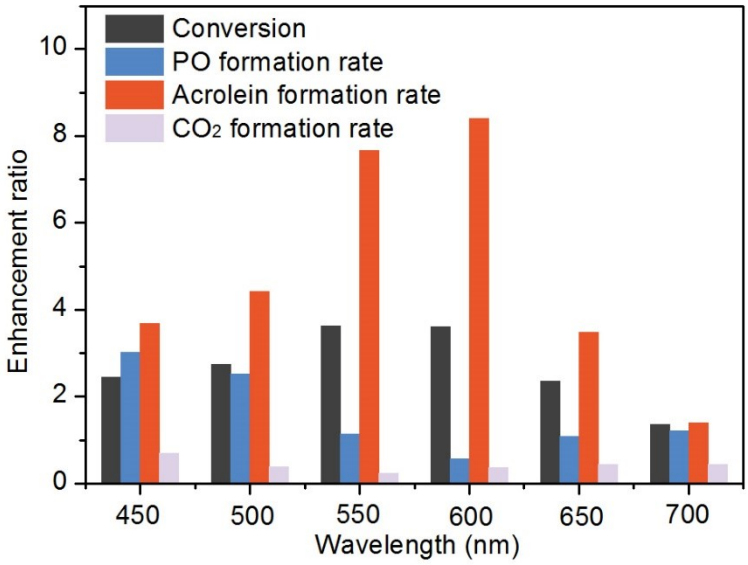

Fig. S29. The enhancements of the propylene conversion and the product formation rate for Au-Cu_2O hierarchical structure at 150 ^oC as a function of incident light wavelengths. They are calculated by dividing the conversion or formation rate with illumination by that without illumination.

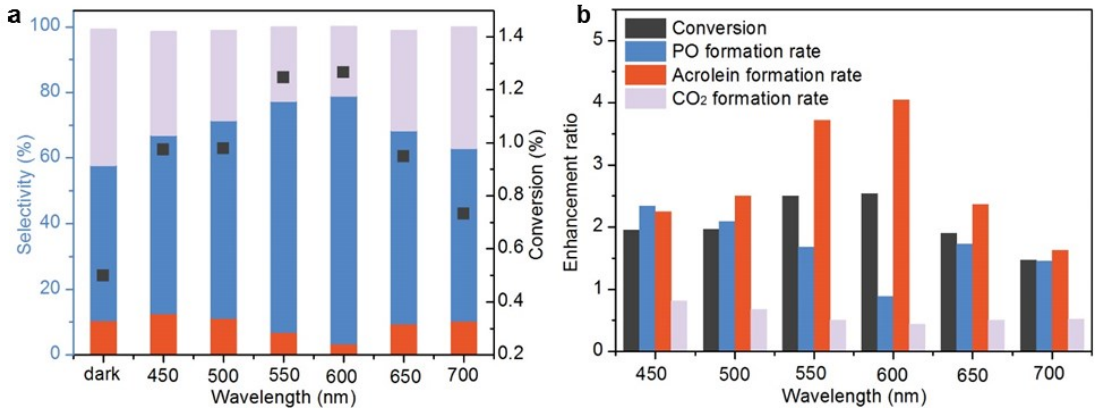

Fig. S30. The catalytic performance (conversion and selectivity) and enhancement ratios for the Au-Cu_2O hierarchical structure at 200 ºC as a function of incident light intensity. (a) The catalytic performance (conversion and selectivity) for the Au-Cu_2O hierarchical structure as a function of incident light wavelength. (b) The enhancements of the propylene conversion and the product formation rate for Au-Cu_2O hierarchical structure at 200 ºC as a function of incident light wavelengths.

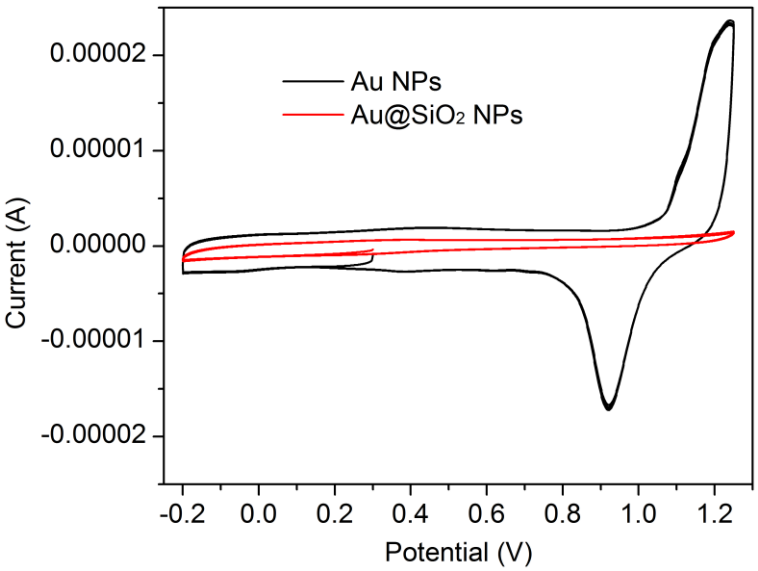

Fig. S31. CV curves of Au NPs or Au@SiO_2 NPs on glassy carbon electrode in 0.1 M H_2SO_4 solution.

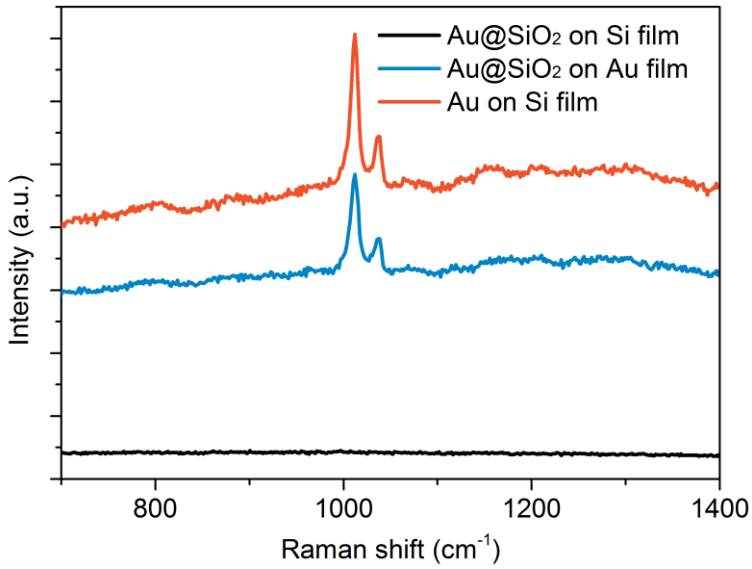

Fig. S32. Raman spectra of pyridine on gold for Au@SiO_2 on Si film, Au@SiO_2 on Au film and Au on Si film systems.

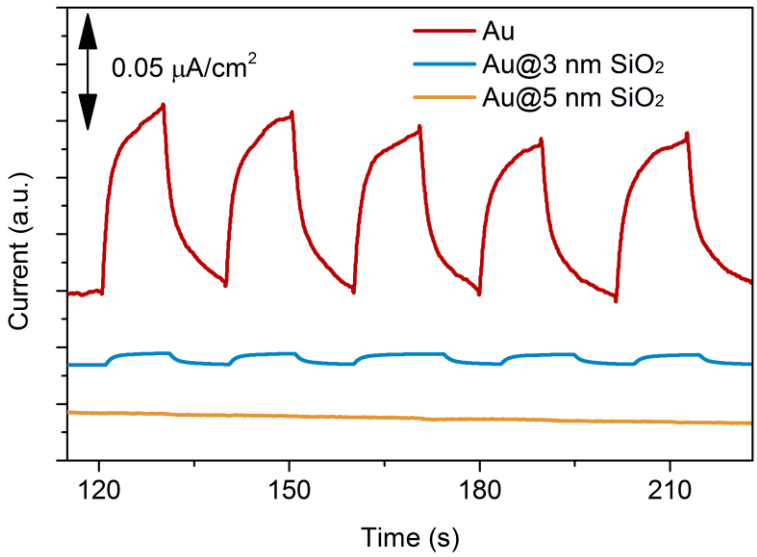

Fig. S33. The photocurrent of Au, Au@SiO_2 3 nm and Au@SiO_2 5nm on glassy carbon electrode in 0.1 M Na_2SO_4 solution at 0.6 V vs SCE.

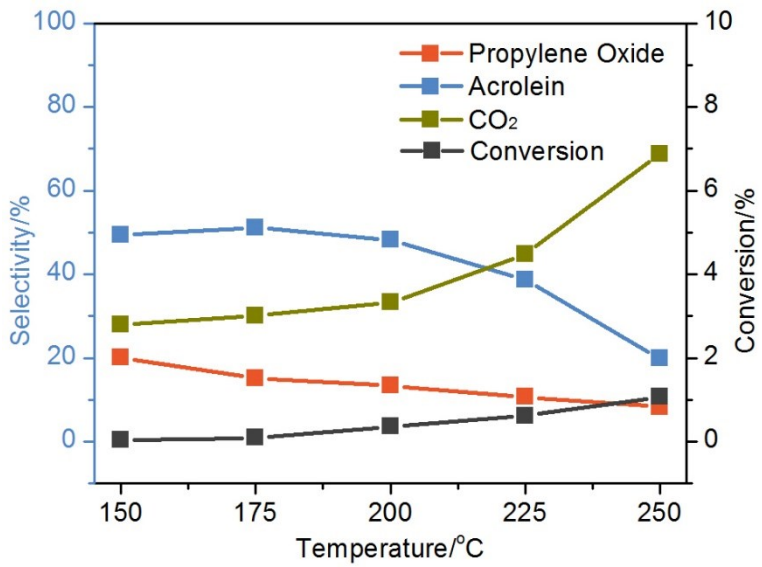

Fig. S34. Catalytic performance of Au@SiO_2-Cu_2O at different temperature. The main product is acrolein.

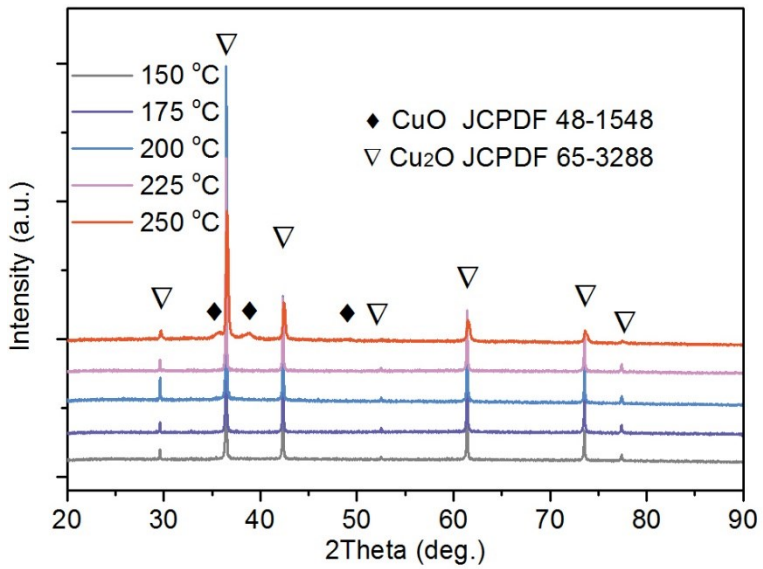

Fig. S35. XRD patterns and of Au@SiO_2-Cu_2O after catalysis at different temperature: (a) 150 °C, (b) 175 °C, (c) 200 °C, (d) 225 °C, (e) 250 °C.

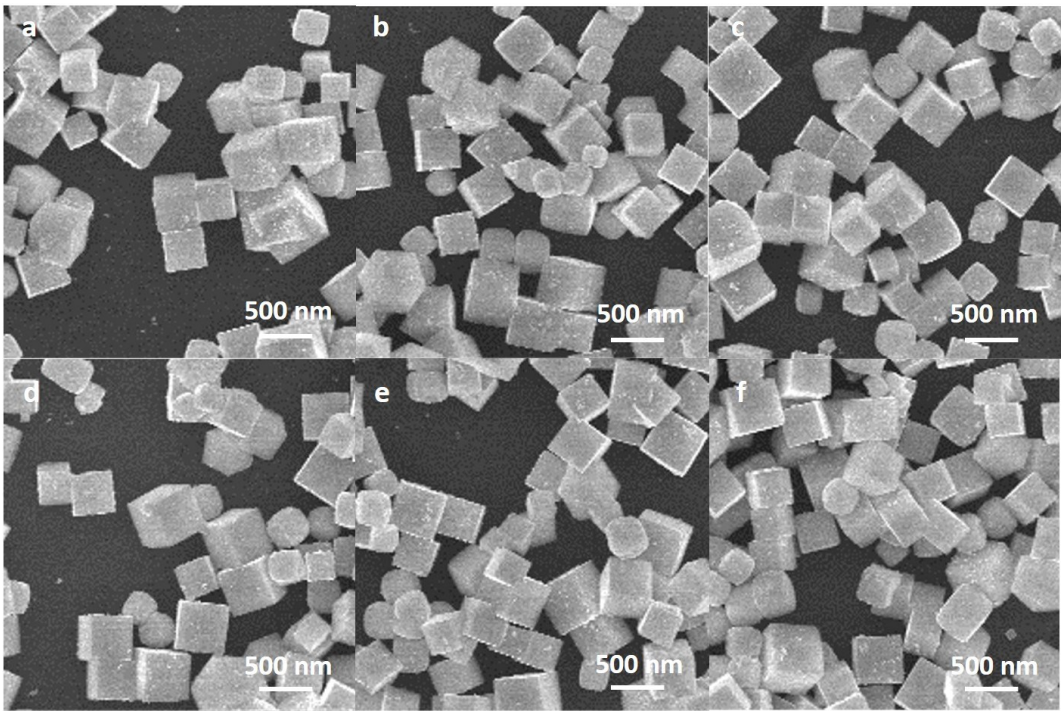

Fig. S36. SEM images of Au@SiO_2-Cu_2O after catalysis at different temperature: (a) 125 °C, (b) 150 °C, (c) 175 °C, (d) 200 °C, (e) 225 °C, (f) 250 °C.

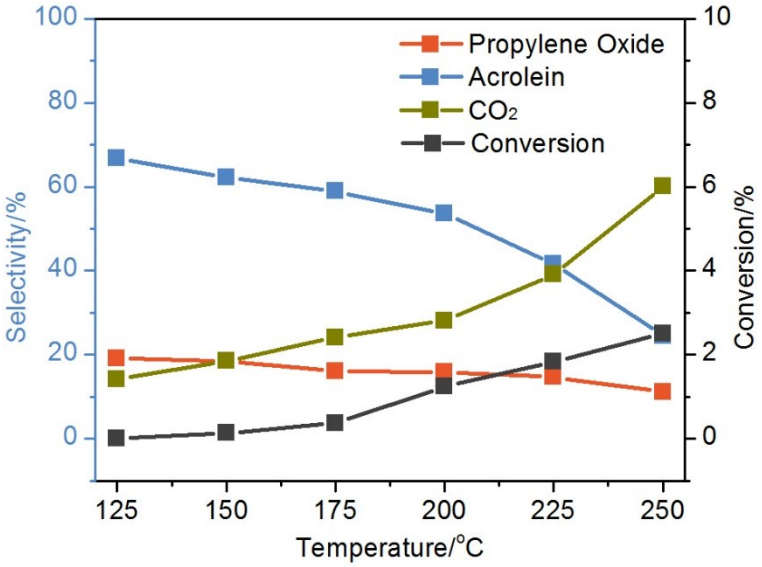

Fig. S37. Catalytic performance of Au@SiO_2-Cu_2O under illumination at different temperature. The main product is acrolein.

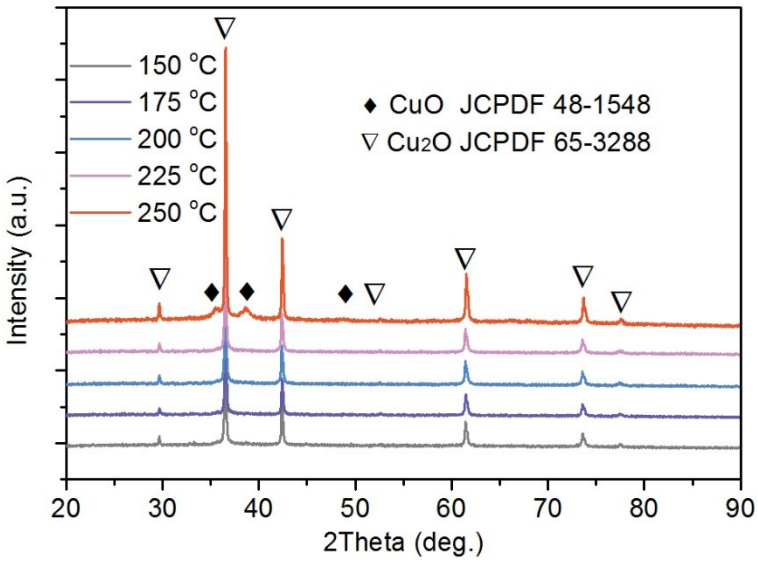

Fig. S38. XRD patterns and of Au@SiO_2-Cu_2O after catalysis under illumination at different temperature: (a) 150 °C, (b) 175 °C, (c) 200 °C, (d) 225 °C, (e) 250 °C.

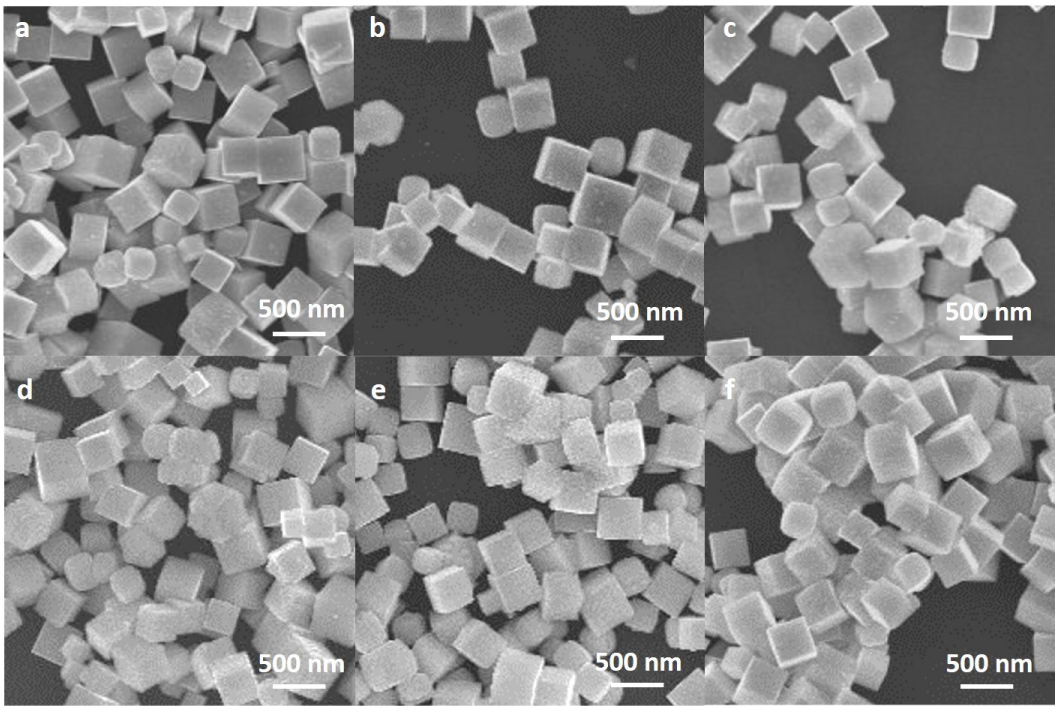

Fig. S39. SEM images of Au@SiO_2-Cu_2O after catalysis under illumination at different temperature: (a) 125 °C, (b) 150 °C, (c) 175 °C, (d) 200 °C, (e) 225 °C, (f) 250 °C.

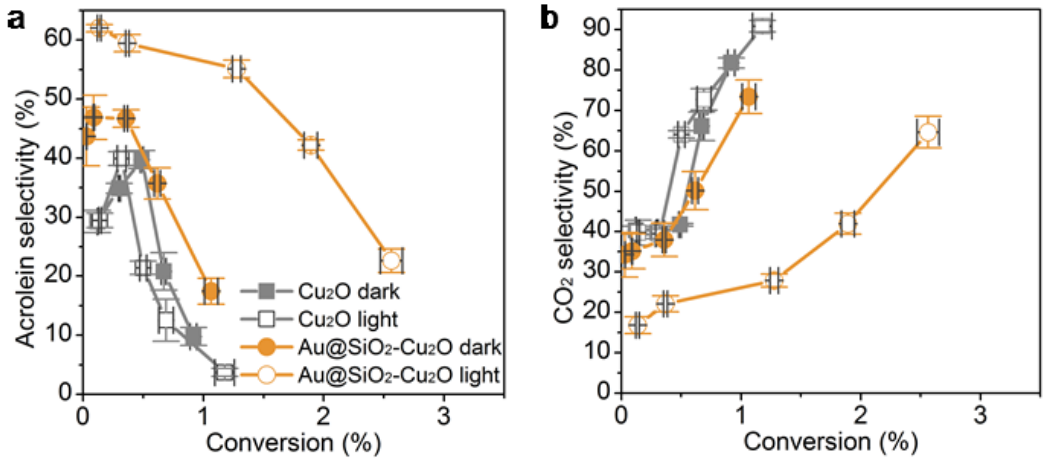

Fig. S40. Catalytic performance of Cu_2O and Au@SiO_2-Cu_2O. a, The selectivity of acrolein catalyzed by Cu_2O (blue) and Au@SiO_2-Cu_2O (red) with and without illumination as a function of propylene conversion. **b**, The selectivity of CO_2 for Cu_2O (blue) and Au@SiO_2-Cu_2O (red) with and without illumination as a function of propylene conversion.

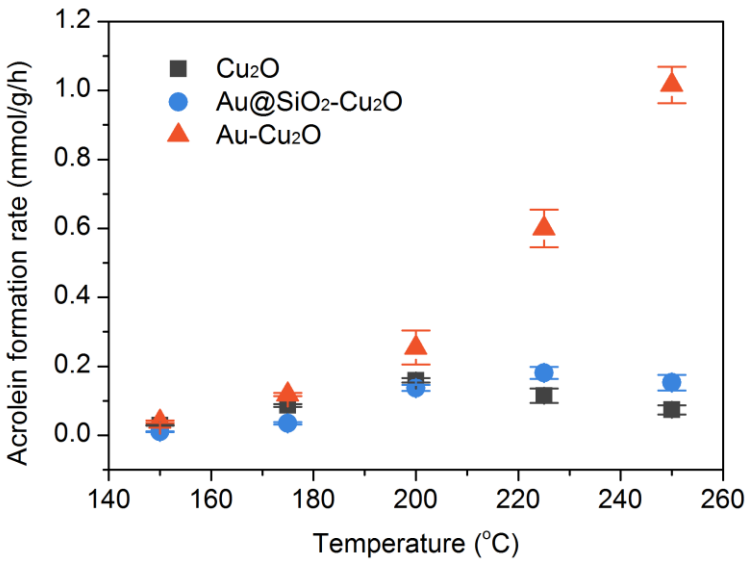

Fig. S41. Temperature dependent acrolein formation rate of Cu_2O, Au@SiO_2-Cu_2O and Au-Cu_2O.

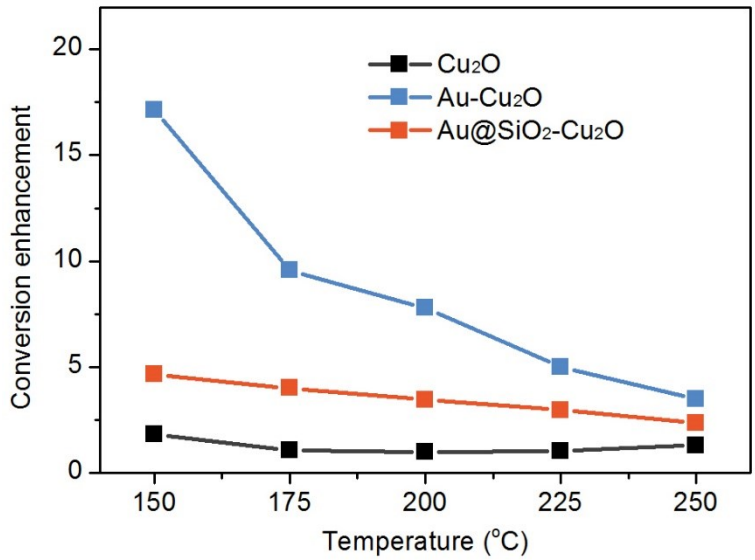

Fig. S42. The conversion enhancements induced by illumination for Cu_2O, Au-Cu_2O and Au@SiO_2-Cu_2O as a function of operating temperature.

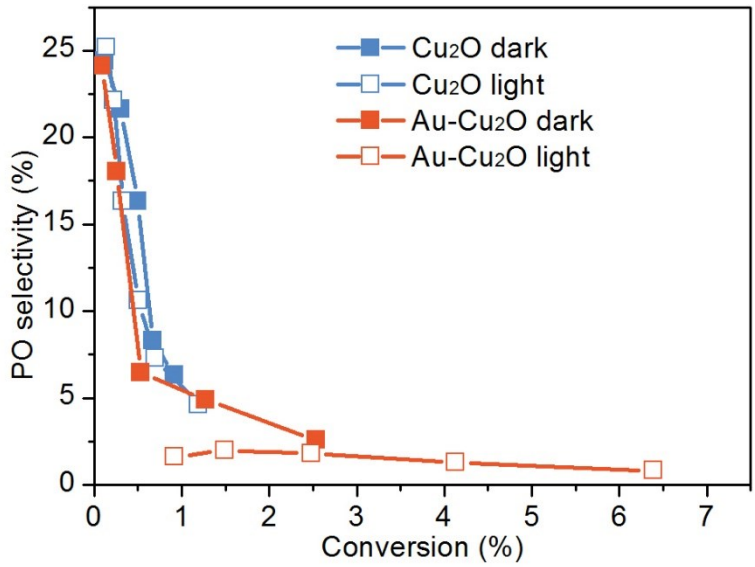

Fig. S43. The selectivity of propylene oxide catalyzed by Cu_2O and Au-Cu_2O with and without illumination as a function of propylene conversion.

Section S2. Theoretical Section

The photo thermal effect and temperature distribution is analyzed using the conventional macroscopic model, which is described by the usual heat transfer equation (*52*): $\rho c\frac{\partial T}{\partial t} = \nabla \cdot (k\nabla T) + Q_0$, where T is the local temperature increase, ρ is mass density, c is heat capacity and k is thermal conductivity. The local heat source density Q_0 origins from the non-radiative energy damping in gold nanoparticles, which writes as $Q_0 =$

$\frac{1}{2}\omega\varepsilon_0\varepsilon''_{au}|E_\omega|^2$, where ω is angular frequency of incident photon, ε_0 is the vacuum permittivity, ε''_{au} is the imaginary part of the relative permittivity of gold adopted from Johnson and Christy's experimental data (*53*), and E_ω the local electric field derived from electromagnetic simulations. In the experimental condition, the illumination time is in tens of minutes, which is much longer than thermal relaxation times, therefore equation can be simplified as the Poisson's equation: $\nabla^2 T = -\frac{Q_0}{k}$. In homogenous medium, the stationary solutions of the equation involve the thermal Green's function and a Dirac source inside particles (*46*). The parameters used in the calculation is listed in Table S1.

Table S1. Parameters used in the calculations (*59*)

Materials	Refractive index, n	Thermal conductivity, k(W/m · k)
Gold	Ref. (*53*)	132.08
Cuprous (I) oxide	Ref. (*59*)	1.07
Helium	1	0.144

We begin with the analysis of single gold particle on cuprous (I) oxide substrate. As shown in figure S44, under normal incidence excitation, the electric field is strongly localized in the vicinity of particle-substrate gap. The confinement or field spatial resolution is about 20 nm, which is highly connected with the curvature of particle (here is the radius of gold sphere). Under asymmetric excitation condition, i.e. oblique incidence with a certain angle, the field will be further localized and enhanced. Figure S45 show a case of incident angles of 30°, yielding the confinement of field down to 6 nm.

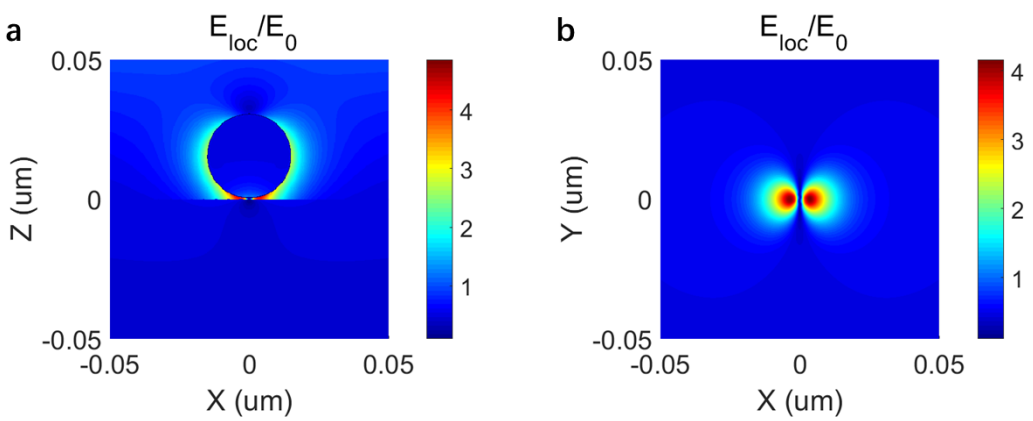

Fig. S44. The local electric field distribution, under normal incident from top to bottom. a) side view, the electric field is highly confined at the particle-substrate gap and forming electromagnetic hotspot, the air-substrate interface is at z = 0 plane. b) Electric

field in the surface of substrate, show a symmetrical dipole-like pattern due to the symmetrical excitation.

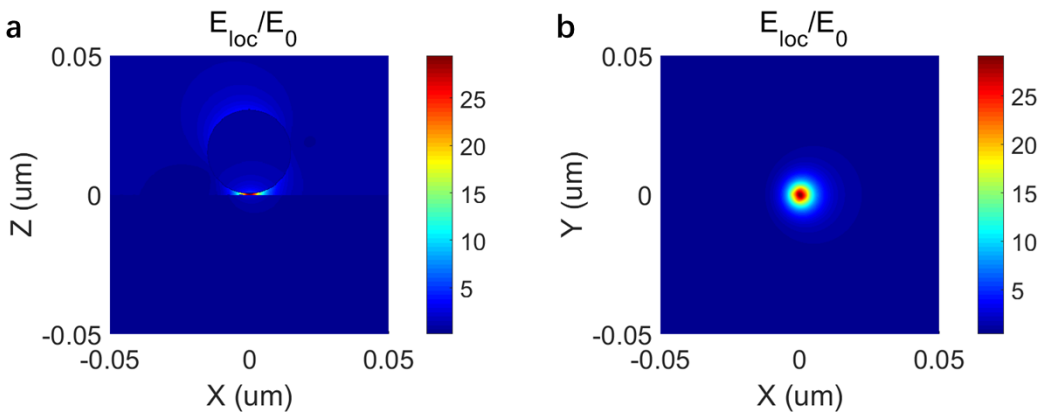

Fig. S45. The local field distribution under oblique incidence with an angle of 30°. a) side view, the field in localized in hotspots, with a maximal enhancement 25 times. b) top view, the electric field at the surface of substrate further enhanced and confined due to the breaking of symmetry.

The temperature distribution can be derived via solving the heat transfer equation in steady-state. The results shown in figure S46 indicate a modest temperature increase of temperature of only 0.8 K, and the maximal temperature increase located at the surface of nanoparticles. Since there are no other heat sources in the surrounding medium and the thermal conductivity of particle is much higher than conductivity of medium, the temperature is almost uniform inside the particle and thermal field also show a confinement in the vicinity of nanoparticle surface and slowly decays in the medium. Figure S46c compare the distribution of temperature, and electric field under normal and oblique incidence, the thermal field show a much weaker confinement than electric case. The rate of most chemical reactions follows the Arrhenius low, hence, the reaction is much easier to trigger at the interface of particle and substrate with both higher temperature and catalytic surface. We assume this active nano region is within 2 nm above the substrate and extract temperature distribution at this cross section, as shown in figure S46b and S46d. The results show a negligible temperature jump (~ 0.07 K) when approaching the particle surface. With such a modest temperature increase and local temperature jump, we will not expect any accelerated reactions.

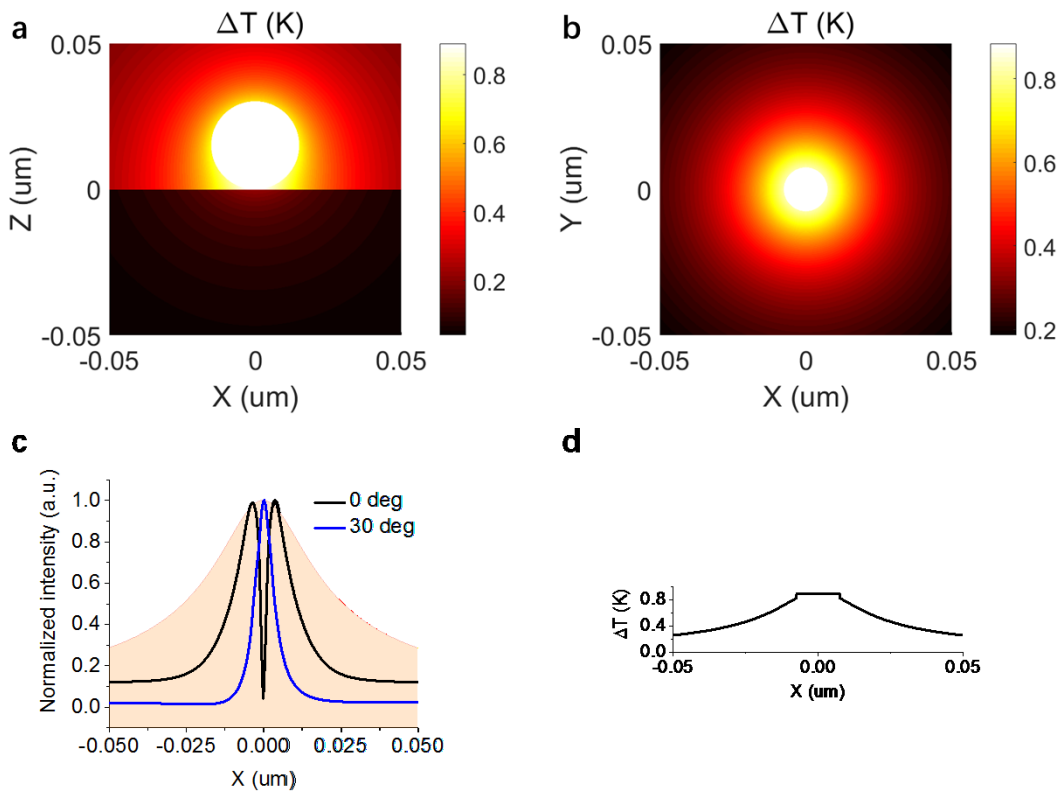

Fig. S46. Photo thermal effect induced by single gold particle. a) Side view of temperature distribution, the gas-substrate interface is at z = 0 plane. b) top view of temperature distribution, to show the temperature of nanoparticle surface, the cutting cross section is at z = 2 nm plane. c) Comparison of temperature (shown in light yellow), electric field under normal incidence (black solid line) and oblique incidence (blue solid line), at the surface of substrate. d) Temperature distribution at the surface of 2 nm above substrate, show a slight jump near particle region.

The mismatch between theory and experiments is also discussed in many photo thermal systems in nanoscale, i.e. solar steam generation (*60, 61*). One explanation is that the macroscopic model neglect of the interfacial thermal resistance between the particle and the surrounding medium (*46, 61, 62*), which is particularly important at the nanoscale.

For example, the surface potential can induce a vibrational energy shift of molecules adsorbed on gold surface, and the mismatch of the vibrational energies of an inner layer of molecules that attach particles and a layer away from particle surface can prevent the energy transfer hence block the heat flow (*61, 63*). In our case, a thermal insulting layer can be introduced due to adsorption of reactive C_3H_6 molecules, and resulting in the heat localization.

We compare the temperature distribution with and without thermal barrier layer. The results in shown in figure S47. For nanoparticle without thermal barrier, the thermal field is diffused and the temperature increase is limited, as shown in figure S47a. While for particle with thermal barrier (figure S47b, S47c), the heat is highly localized around

particle surface due to the insulting of energy exchange, and in the vicinity of particle surface, an abrupt temperature jump is observed. One can infer that the reactive molecules enriched on the surface of particles as well as substrate, and yielding a thermal insulting layer that block the heat flow and forming a high temperature region that highly localized around the surface of nanoparticles.

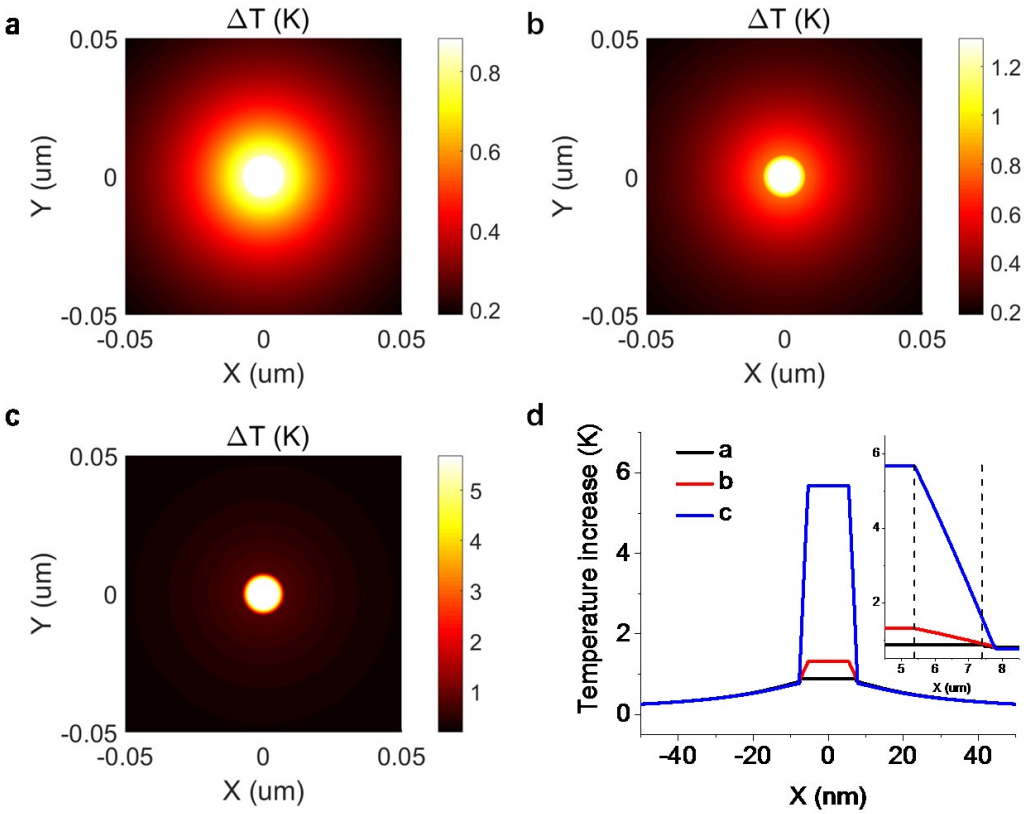

Fig. S47. The influence of surface thermal barrier. Temperature distribution at the surface of 2 nm above substrate, without surface thermal barrier layer (a), with 1 nm thermal barrier layer and the thermal conductivity equals to conductivity of C_3H_6 gas (b), with 1 nm thermal barrier layer and the thermal conductivity is one tenth of conductivity of C_3H_6 gas (c). (d) Temperature distribution along x direction of case in figure a (black solid line), b (red solid line) and c (blue solid line), respectively. The inset is a zoom in in figure d around the particle surface region, show an obvious temperature jump.

We have to emphasize that when a large amount of particles is illuminated, the temperature profile can be distinct from single particle situation, due to the thermal collective effect (*64, 65*). The temperature can become uniform throughout the particles, although the heat sources are localized. We analysis the collective heating effect via simulating 121 particles that assembled with varied periodicity, which reflect the surface density of particle numbers, as shown in figure S48. In a low particle density, as shown in figure S48a, the temperature is localized around particles and the temperature increase of surrounding medium is limited. While in a high particle density, as shown in figure S48c,

the temperature is no longer localized to the surface of particles, and we can observe a significant temperature increase of surrounding medium. In our experimental condition, the surface particle density can be approximately estimated from the SEM images, in which show a moderate number of 100 – 300/ μm^2. Therefore, we can safely claim that the localization of temperature still holds in our case, as shown in figure S48b.

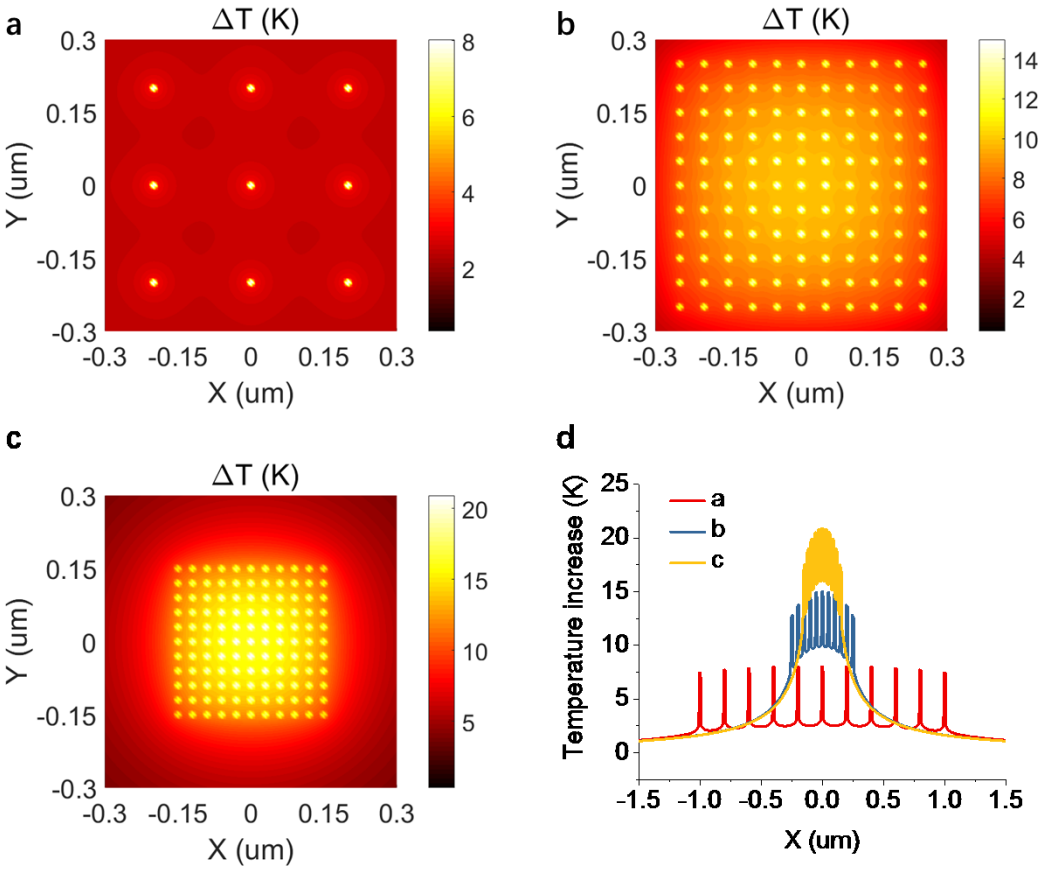

Fig. S48. Collective heating effect with different particle concentration. Here we used 11×11 particle array with varied periodicity to simulate the multi-particles on substrate surface. (a) The Temperature distribution with a low surface particle density of 25/μm^2, the temperature field is localized in the vicinity of particle. (b) Temperature distribution with a moderate surface particle density of 300/μm^2, the collective heating effect yielding an obvious temperature raise in surrounding medium. (c) Temperature distribution with a high surface particle density of 1300/μm^2, the temperature is delocalized with a high temperature increase surrounding medium. (d) Temperature distribution along x direction, shown in figure a (red solid line) and b (blue solid line) and c (yellow solid line).

REFERENCES AND NOTES

1. B. Hammer, J. K. Norskov, Why gold is the noblest of all the metals. *Nature* **376**, 238–240 (1995).

2. A. Wittstock, V. Zielasek, J. Biener, C. M. Friend, M. Bäumer, Nanoporous gold catalysts for selective gas-phase oxidative coupling of methanol at low temperature. *Science* **327**, 319–322 (2010).

3. J. Huang, M. Haruta, Gas-phase propene epoxidation over coinage metal catalysts. *Res. Chem. Intermed.* **38**, 1–24 (2012).

4. E. C. Tyo, S. Vajda, Catalysis by clusters with precise numbers of atoms. *Nat. Nano.* **10**, 577–588 (2015).

5. C. T. Campbell, S. C. Parker, D. E. Starr, The effect of size-dependent nanoparticle energetics on catalyst sintering. *Science* **298**, 811–814 (2002).

6. J. A. Schuller, E. S. Barnard, W. Cai, Y. C. Jun, J. S. White, M. L. Brongersma, Plasmonics for extreme light concentration and manipulation. *Nat. Mater.* **9**, 193–204 (2010).

7. J. J. Baumberg, J. Aizpurua, M. H. Mikkelsen, D. R. Smith, Extreme nanophotonics from ultrathin metallic gaps. *Nat. Mater.* **18**, 668–678 (2019).

8. C. Zhan, X.-J. Chen, J. Yi, J.-F. Li, D.-Y. Wu, Z.-Q. Tian, From plasmon-enhanced molecular spectroscopy to plasmon-mediated chemical reactions. *Nat. Rev. Chem.* **2**, 216–230 (2018).

9. F. Neubrech, X. Duan, N. Liu, Dynamic plasmonic color generation enabled by functional materials. *Sci. Adv.* **6**, eabc2709 (2020).

10. S. Mubeen, J. Lee, N. Singh, S. Kramer, G. D. Stucky, M. Moskovits, An autonomous photosynthetic device in which all charge carriers derive from surface plasmons. *Nat. Nanotech.* **8**, 247–251 (2013).

11. D. F. Swearer, H. Zhao, L. Zhou, C. Zhang, H. Robatjazi, J. M. P. Martirez, C. M. Krauter, S. Yazdi, M. J. McClain, E. Ringe, E. A. Carter, P. Nordlander, N. J. Halas, Heterometallic antenna–reactor complexes for photocatalysis. *Proc. Nat. Acad. Sci. U.S.A.* **113**, 8916–8920 (2016).

12. A. Marimuthu, J. Zhang, S. Linic, Tuning selectivity in propylene epoxidation by plasmon mediated photo-switching of Cu oxidation state. *Science* **339**, 1590–1593 (2013).

13. L. Zhou, D. F. Swearer, C. Zhang, H. Robatjazi, H. Zhao, L. Henderson, L. Dong, P. Christopher, E. A. Carter, P. Nordlander, N. J. Halas, Quantifying hot carrier and thermal contributions in plasmonic photocatalysis. *Science* **362**, 69–72 (2018).

14. Y. Kim, J. G. Smith, P. K. Jain, Harvesting multiple electron–hole pairs generated through plasmonic excitation of Au nanoparticles. *Nat. Chem.* **10**, 763–769 (2018).

15. T. Oshikiri, K. Ueno, H. Misawa, Plasmon-induced ammonia synthesis through nitrogen photofixation with visible light irradiation. *Angew. Chem. Int. Ed.* **53**, 9802–9805 (2014).

16. C. Zhan, Z.-Y. Wang, X.-G. Zhang, X.-J. Chen, Y.-F. Huang, S. Hu, J.-F. Li, D.-Y. Wu, M. Moskovits, Z.-Q. Tian, Interfacial construction of plasmonic nanostructures for the utilization of the plasmon-excited electrons and holes. *J. Am. Chem. Soc.* **141**, 8053–8057 (2019).

17. A. Tittl, X. Yin, H. Giessen, X.-D. Tian, Z.-Q. Tian, C. Kremers, D. N. Chigrin, N. Liu, Plasmonic smart dust for probing local chemical reactions. *Nano Lett.* **13**, 1816–1821 (2013).

18. B. Munkhbat, M. Wersäll, D. G. Baranov, T. J. Antosiewicz, T. Shegai, Suppression of photo-oxidation of organic chromophores by strong coupling to plasmonic nanoantennas. *Sci. Adv.* **4**, eaas9552 (2018).

19. C. Clavero, Plasmon-induced hot-electron generation at nanoparticle/metal-oxide interfaces for photovoltaic and photocatalytic devices. *Nat. Photonics* **8**, 95–103 (2014).

20. M. L. Brongersma, N. J. Halas, P. Nordlander, Plasmon-induced hot carrier science and technology. *Nat. Nanotech.* **10**, 25–34 (2015).

21. P. Christopher, M. Moskovits, Hot charge carrier transmission from plasmonic nanostructures. *Annu. Rev. Phys. Chem.* **68**, 379–398 (2017).

22. J. Li, S. K. Cushing, F. Meng, T. R. Senty, A. D. Bristow, N. Wu, Plasmon-induced resonance energy transfer for solar energy conversion. *Nat. Photonics* **9**, 601–607 (2015).

23. J. J. Baumberg, Hot electron science in plasmonics and catalysis: What we argue about. *Faraday Discuss.* **214**, 501–511 (2019).

24. J. S. DuChene, G. Tagliabue, A. J. Welch, W.-H. Cheng, H. A. Atwater, Hot hole collection and photoelectrochemical CO_2 reduction with plasmonic Au/p-GaN photocathodes. *Nano Lett.* **18**, 2545–2550 (2018).

25. S. Linic, U. Aslam, C. Boerigter, M. Morabito, Photochemical transformations on plasmonic metal nanoparticles. *Nat. Mater.* **14**, 567–576 (2015).

26. U. Aslam, V. G. Rao, S. Chavez, S. Linic, Catalytic conversion of solar to chemical energy on plasmonic metal nanostructures. *Nat. Catal.* **1**, 656–665 (2018).

27. Y. Zhang, S. He, W. Guo, Y. Hu, J. Huang, J. R. Mulcahy, W. D. Wei, Surface-plasmon-driven hot electron photochemistry. *Chem. Rev.* **118**, 2927–2954 (2018).

28. G. Baffou, R. Quidant, Nanoplasmonics for chemistry. *Chem. Soc. Rev.* **43**, 3898–3907 (2014).

29. P. Christopher, H. Xin, S. Linic, Visible-light-enhanced catalytic oxidation reactions on plasmonic silver nanostructures. *Nat. Chem.* **3**, 467–472 (2011).

30. Y.-F. Huang, M. Zhang, L.-B. Zhao, J.-M. Feng, D.-Y. Wu, B. Ren, Z.-Q. Tian, Activation of oxygen on gold and silver nanoparticles assisted by surface plasmon resonances. *Angew. Chem. Int. Ed.* **53**, 2353–2357 (2014).

31. P. Christopher, H. Xin, A. Marimuthu, S. Linic, Singular characteristics and unique chemical bond activation mechanisms of photocatalytic reactions on plasmonic nanostructures. *Nat. Mater.* **11**, 1044–1050 (2012).

32. E. Cortés, W. Xie, J. Cambiasso, A. S. Jermyn, R. Sundararaman, P. Narang, S. Schlücker, S. A. Maier, Plasmonic hot electron transport drives nano-localized chemistry. *Nat. Commun.* **8**, 14880 (2017).

33. E. Kazuma, J. Jung, H. Ueba, M. Trenary, Y. Kim, Real-space and real-time observation of a plasmon-induced chemical reaction of a single molecule. *Science* **360**, 521–526 (2018).

34. W.-C. D. Yang, C. Wang, L. A. Fredin, P. A. Lin, L. Shimomoto, H. J. Lezec, R. Sharma, Site-selective CO disproportionation mediated by localized surface plasmon resonance excited by electron beam. *Nat. Mater.* **18**, 614–619 (2019).

35. U. Aslam, S. Chavez, S. Linic, Controlling energy flow in multimetallic nanostructures for plasmonic catalysis. *Nat. Nanotech.* **12**, 1000–1005 (2017).

36. L. Zhou, J. M. P. Martirez, J. Finzel, C. Zhang, D. F. Swearer, S. Tian, H. Robatjazi, M. Lou, L. Dong, L. Henderson, P. Christopher, E. A. Carter, P. Nordlander, N. J. Halas, Light-driven methane dry reforming with single atomic site antenna-reactor plasmonic photocatalysts. *Nat. Energy* **5**, 61–70 (2020).

37. D. Torres, N. Lopez, F. Illas, R. M. Lambert, Low-basicity oxygen atoms: A key in the search for propylene epoxidation catalysts. *Angew. Chem. Int. Ed.* **46**, 2055–2058 (2007).

38. W. Zhu, Q. Zhang, Y. Wang, Cu(I)-catalyzed epoxidation of propylene by molecular oxygen. *J. Phys. Chem. C* **112**, 7731–7734 (2008).

39. Q. Hua, T. Cao, X.-K. Gu, J. Lu, Z. Jiang, X. Pan, L. Luo, W.-X. Li, W. Huang, Crystal-plane-controlled selectivity of Cu_2O catalysts in propylene oxidation with molecular oxygen. *Angew. Chem. Int. Ed.* **53**, 4856–4861 (2014).

40. R. L. Myers, *The 100 Most Important Chemical Compounds* (Greenwood Press, 2007).

41. Y. Wang, H. Chu, W. Zhu, Q. Zhang, Copper-based efficient catalysts for propylene epoxidation by molecular oxygen. *Catal. Today* **131**, 496–504 (2008).

42. G. Schwab, K. Koller, Combined action of metal and semiconductor catalysts. *J. Am. Chem. Soc.* **90**, 3078–3080 (1968).

43. J. Y. Park, L. R. Baker, G. A. Somorjai, Role of hot electrons and metal–oxide interfaces in surface chemistry and catalytic reactions. *Chem. Rev.* **115**, 2781–2817 (2015).

44. E. Pensa, J. Gargiulo, A. Lauri, S. Schlücker, E. Cortés, S. A. Maier, Spectral screening of the energy of hot holes over a particle plasmon resonance. *Nano Lett.* **19**, 1867–1874 (2019).

45. B. Y. Zheng, H. Zhao, A. Manjavacas, M. McClain, P. Nordlander, N. J. Halas, Distinguishing between plasmon-induced and photoexcited carriers in a device geometry. *Nat. Commun.* **6**, 7797 (2015).

46. G. Baffou, R. Quidant, C. Girard, Thermoplasmonics modeling: A Green's function approach. *Phys. Rev. B* **82**, 165424 (2010).

47. N. J. Hogan, A. S. Urban, C. Ayala-Orozco, A. Pimpinelli, P. Nordlander, N. J. Halas, Nanoparticles heat through light localization. *Nano Lett.* **14**, 4640–4645 (2014).

48. H. Robatjazi, H. Zhao, D. F. Swearer, N. J. Hogan, L. Zhou, A. Alabastri, M. J. McClain, P. Nordlander, N. J. Halas, Plasmon-induced selective carbon dioxide conversion on earth-abundant aluminum-cuprous oxide antenna-reactor nanoparticles. *Nat. Commun.* **8**, 27 (2017).

49. G. Frens, Controlled nucleation for the regulation of the particle size in monodisperse gold suspensions. *Nat. Phys. Sci.* **241**, 20–22 (1973).

50. J. F. Li, Y. F. Huang, Y. Ding, Z. L. Yang, S. B. Li, X. S. Zhou, F. R. Fan, W. Zhang, Z. Y. Zhou, D. Y. Wu, B. Ren, Z. L. Wang, Z. Q. Tian, Shell-isolated nanoparticle-enhanced Raman spectroscopy. *Nature* **464**, 392–395 (2010).

51. J. Wen, H. Wang, W. Wang, Z. Deng, C. Zhuang, Y. Zhang, F. Liu, J. She, J. Chen, H. Chen, S. Deng, N. Xu, Room-temperature strong light–matter interaction with active control in single plasmonic nanorod coupled with two-dimensional atomic crystals. *Nano Lett.* **17**, 4689–4697 (2017).

52. A. O. Govorov, W. Zhang, T. Skeini, H. Richardson, J. Lee, N. A. Kotov, Gold nanoparticle ensembles as heaters and actuators: Melting and collective plasmon resonances. *Nano. Res. Lett.* **1**, 84–90 (2006).

53. P. B. Johnson, R. W. Christy, Optical constants of the noble metals. *Phys. Rev. B* **6**, 4370–4379 (1972).

54. J. Ghijsen, L. H. Tjeng, J. van Elp, H. Eskes, J. Westerink, G. A. Sawatzky, M. T. Czyzyk, Electronic structure of Cu_2O and CuO. *Phys. Rev. B* **38**, 11322–11330 (1988).

55. S. Poulston, P. M. Parlett, P. Stone, M. Bowker, Surface oxidation and reduction of CuO and Cu2O studied using XPS and XAES. *Surf. Interface Anal.* **24**, 811–820 (1996).

56. N. Kruse, S. Chenakin, XPS characterization of Au/TiO_2 catalysts: Binding energy assessment and irradiation effects. *Appl. Catal. A* **391**, 367–376 (2011).

57. I. Tunc, S. Suzer, M. A. Correa-Duarte, L. M. Liz-Marzán, XPS characterization of Au (core)/SiO2 (shell) nanoparticles. *J. Phys. Chem. B* **109**, 7597–7600 (2005).

58. C. Zhan, B.-W. Liu, Y.-F. Huang, S. Hu, B. Ren, M. Moskovits, Z.-Q. Tian, Disentangling charge carrier from photothermal effects in plasmonic metal nanostructures. *Nat. Commun.* **10**, 2671 (2019).

59. E. D. Palik, *Handbook of Optical Constants of Solids* (Academic press, 1998), vol. 3.

60. H. Ghasemi, G. Ni, A. M. Marconnet, J. Loomis, S. Yerci, N. Miljkovic, G. Chen, Solar steam generation by heat localization. *Nat. Commun.* **5**, 4449 (2014).

61. O. Neumann, A. S. Urban, J. Day, S. Lal, P. Nordlander, N. J. Halas, Solar vapor generation enabled by nanoparticles. *ACS Nano* **7**, 42–49 (2013).

62. J. Alpert, K. Hamad-Schifferli, Effect of ligands on thermal dissipation from gold nanorods. *Langmuir* **26**, 3786–3789 (2010).

63. J. A. Eastman, S. R. Phillpot, S. U. S. Choi, P. Keblinski, Thermal transport in nanofluids. *Annu. Rev. Mater. Chem.* **34**, 219–246 (2004).

64. H. H. Richardson, M. T. Carlson, P. J. Tandler, P. Hernandez, A. O. Govorov, Experimental and theoretical studies of light-to-heat conversion and collective heating effects in metal nanoparticle solutions. *Nano Lett.* **9**, 1139–1146 (2009).

65. G. Baffou, P. Berto, E. Bermúdez Ureña, R. Quidant, S. Monneret, J. Polleux, H. Rigneault, Photoinduced heating of nanoparticle arrays. *ACS Nano* **7**, 6478–6488 (2013).